RL-TR-96-228
Final Technical Report
February 1997

ADVANCED SENSOR SIGNAL PROCESSING USING OPTICAL TECHNIQUES

Essex Corporation

DTIC QUALITY INSPECTED 2
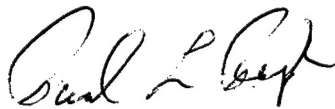
19970324 023

**Rome Laboratory
Air Force Materiel Command
Rome, New York**

This report has been reviewed by the Rome Laboratory Public Affairs Office (PA) and is releasable to the National Technical Information Service (NTIS). At NTIS it will be releasable to the general public, including foreign nations.
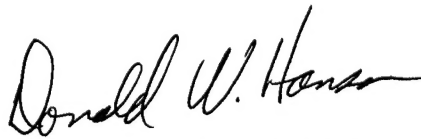
RL-TR-96-228 has been reviewed and is approved for publication.

APPROVED:

PAUL L. REPAK
Project Engineer

FOR THE COMMANDER:

DONALD W. HANSON, Director
Surveillance & Photonics Directorate

ADVANCED SENSOR SIGNAL PROCESSING
USING OPTICAL TECHNIQUES

Contractor: Essex Corporation
Contract Number: F30602-95-C-0252
Effective Date of Contract: 8 September 1995
Contract Expiration Date: 8 September 1996
Program Code Number: 5L10
Short Title of Work: Advanced Sensor Signal Processing
Using Optical Techniques
Period of Work Covered: Sep 95 - Sep 96

Principal Investigator: William R. Franklin
Phone: (301) 953-7797
RL Project Engineer: Paul L. Repak
Phone: (315) 330-03146

REPORT DOCUMENTATION PAGE

Form Approved
OMB No. 0704-0188

1. AGENCY USE ONLY (Leave Blank)	2. REPORT DATE February 1997	3. REPORT TYPE AND DATES COVERED FINAL SEP 95 – SEP 96

4. TITLE AND SUBTITLE	5. FUNDING NUMBERS
ADVANCED SENSOR SIGNAL PROCESSING USING OPTICAL TECHNIQUES	C - F30602-95-C-0252 PE - 63226E
6. AUTHOR(S) Laurence A. Eichel William R. Franklin, Ph.D., Leslie H. Gesell, Ph.D., Stephen Evanko, Robert Kallman, Ph.D., Robert Bowden,	PR - C992 TA - 00 WU - 01

7. PERFORMING ORGANIZATION NAME(S) AND ADDRESS(ES) Essex Corporation Federal Systems Division 9150 Guilford Road Columbia MD 21046-1891	8. PERFORMING ORGANIZATION REPORT NUMBER N/A

9. SPONSORING/MONITORING AGENCY NAME(S) AND ADDRESS(ES) Advanced Research Projects Agency 3701 North Airfax Drive Arlington VA 22203-1714 Rome Laboratory/OCPC 25 Electronic Pky Rome NY 13441-4514	10. SPONSORING/MONITORING AGENCY REPORT NUMBER RL-TR-96-228

11. SUPPLEMENTARY NOTES

Rome Laboratory Project Engineer: Paul L. Repak/RL/OCPC/(315)330-3146

12a. DISTRIBUTION/AVAILABILITY STATEMENT Approved for public release; distribution unlimited	12b. DISTRIBUTION CODE

13. ABSTRACT (Maximum 200 words)

A Fourier transform based iterative technique is presented for solution of Toeplitz and general matrix equations resulting in an algorithm for the determination of an adaptive beam steering vector from the radar covariance matrix. An associated optoelectronic architecture is offered that computer simulation shows will be more than forty times faster that plausible all-digital alternatives. A quantitative comparison is made between i860 based architectures and the patented ImSyn^{TM} optoelectronic processor for the formation of SAR images. It is shown that the ImSyn^{TM} processor meets or exceeds all requirements for current and next generation SAR in a package that is smaller, lighter and that consumes less power than the all-digital devices. Complex valued spatial filters are developed for SAR ATR using simulated SAR images. When implemented on the ImSyn^{TM} processor, a high degree of discrimination is demonstrated even between quite similar targets. Optoelectronic implementation of the maximum energy recovery algorithm (MERA) is studied for the tracking of sub-pixel moving targets. System parameters are given and it is found that most components are or will be commercially available.

14. SUBJECT TERMS ATR, correlation, Fourier transform, MERA, optoelectronics, radar, sensors, signal processing, STAP			15. NUMBER OF PAGES 84
			16. PRICE CODE

17. SECURITY CLASSIFICATION OF REPORT UNCLASSIFIED	18. SECURITY CLASSIFICATION OF THIS PAGE UNCLASSIFIED	19. SECURITY CLASSIFICATION OF ABSTRACT UNCLASSIFIED	20. LIMITATION OF ABSTRACT UNLIMITED

List of Figures

List of Tables

1. Summary

1.1 Project Objectives and Scope

The general purpose of this effort has been to demonstrate the advantages of optoelectronics in advanced radar signal processing. Because optoelectronic processors offer enormous computing power in packages which are smaller, lighter, less expensive and consume less power than equivalent all-digital implementations, there is much reason to suspect that many such advantages could be found.

The research carried out under this contract, summarized briefly in this section, and in far more detail in the following sections, was achieved by mathematical analyses and computer simulations.

1.2 Major Achievements

The work reported here was divided into four principal areas which are discussed below and arranged in approximately descending order of level of priority.

1.2.1 Space Time Adaptive Processing (STAP) (SOW 4.1.1)

Solution of linear systems of equations, particularly inversion of the radar covariance matrix to compute an adaptive steering vector, was examined in the context of optoelectronic processors. To admit a Fourier transform technique for matrix inversion, replacement of the covariance matrix by a circulant approximation using various optimal and superoptimal preconditioners for both Toeplitz and general matrices was studied. When followed by an iterative technique to achieve desired accuracy, this resulted in a computationally efficient algorithm that has both optoelectronic and all-digital implementations. Further, a number of optoelectronic architectures were defined that solve such systems of equations in a manner that promises to be more than forty times faster, in terms of iteration loop period, than plausible all-digital alternatives.

1.2.2 SAR Image Formation (SOW 4.1.2)

In this task, the *ImSyn*™ Processor, designed and patented by Essex Corporation, was compared with a variety of i860 based architectures for SAR image formation. It was found that the *ImSyn*™ Processor can meet or exceed the requirements of current and next generation SAR in a package that is smaller, lighter, less expensive and that consumes less power than all competing systems based on the i860.

1

1.2.3 SAR ATR (SOW 4.1.3)

The purpose here was to investigate automatic target recognition (ATR) in synthetic aperture radar (SAR) images using complex valued spatial filters and the *ImSyn*™ Processor as a correlator. Several sets of spatial filters were created based on training sets composed of simulated SAR images. These were implemented on the *ImSyn*™ Processor and a high degree of discrimination between quite similar targets, with and without background, was achieved.

1.2.4 IR and Radar Search and Track (SOW 4.1.4)

The purpose of this task was to provide size, weight and power estimates for an optoelectronic implementation of the Maximum Energy Recovery Algorithm (MERA). Some preliminary hardware issues were resolved and some potential applications to current and future surveillance systems were identified.

2. Task 1 - Space Time Adaptive Processing (STAP) (SOW4.1.1)

2.1 Solution of Toeplitz Systems by Circulant Approximation

Many problems in STAP involve the solution of systems of equations

$$Tx = b$$

where T is a radar covariance matrix, x represents the adaptive steering vector of an antenna array and b represents a non-adaptive steering vector. If T is an n x n matrix, inverting this system by conventional means using, say, Gaussian elimination, requires on the order of n^3 operations. For an antenna array, n is the product of the number of elements in the array and the number of pulses in a coherent processing interval (CPI). Hence, the computational burden for realistic problems rapidly becomes insupportable.

However, if the inversion of a matrix could be cast in terms of Fourier transforms, such a problem might become more tractable since Fourier transforms and operations with them are especially amenable to optical processing. Achieving such a formulation was one of the original goals of this program and its accomplishment is described in this section.

The first step in formulating the approach lies in observing that the matrix T, above, is often Toeplitz, i.e., has the property that:

$$T_{ij} = T_{i-j}.$$

The key to introducing Fourier transforms and discrete convolutions is to replace T by a suitably chosen circulant approximation.

An n x n matrix C is said to be circulant if

$$C_{ij} = C_{(i-j) \bmod n} \, .$$

Any circulant matrix C can be written as

$$C = F^*\Lambda F$$

where F is the discrete Fourier transform matrix whose elements are

$$F_{jk} = \exp(2\pi i jk/n)$$

and Λ is a diagonal matrix containing the eigenvalues of C. The eigenvalues of C are given by

$$\sqrt{n}\, Fc$$

where c is the first column of C.

Multiplication by C is equivalent to discrete convolution, leading to Fourier transform solutions to systems of linear equations. Thus,

$$Cx = b$$

is equivalent to

$$c * x = b.$$

A discrete Fourier transform leads to

$$\chi \xi = \beta$$

(where Greek letters denote Fourier transforms). So, x is found by a component wise division followed by an inverse Fourier transform.

A Toeplitz matrix-vector multiplication can also be achieved by a Fourier transform by embedding the Toeplitz matrix in a circulant matrix of twice the dimension. For example,

$$T = \begin{pmatrix} t_0 & t_{-1} & t_{-2} \\ t_1 & t_0 & t_{-1} \\ t_2 & t_1 & t_0 \end{pmatrix}$$

can be embedded as the leading principal submatrix of

$$C = \begin{pmatrix} t_0 & t_{-1} & t_{-2} & 0 & t_2 & t_1 \\ t_1 & t_0 & t_{-1} & t_{-2} & 0 & t_2 \\ t_2 & t_1 & t_0 & t_{-1} & t_{-2} & 0 \\ 0 & t_2 & t_1 & t_0 & t_{-1} & t_{-2} \\ t_{-2} & 0 & t_2 & t_1 & t_0 & t_{-1} \\ t_{-1} & t_{-2} & 0 & t_2 & t_1 & t_0 \end{pmatrix}.$$

Then,

$$y = Tb$$

is computed using Fourier transforms to form the circulant matrix-vector product

$$\psi = C\begin{pmatrix} b \\ 0 \end{pmatrix}$$

and recovering y as the first n components of ψ. (These and other useful properties of circulant matrices are described, for example, in Ref. 1.)

The goal, then, is to replace the Toeplitz matrix by a circulant in any system to be solved. The circulant should be chosen to be close to T in some sense. One way to achieve this is to chose C to be

$$\min_{C} \|T - C\|_F$$

where $\|\ \|_F$ denotes the Frobenius norm defined by

$$\|A\|_F = \left| \sum_{i,j} A_{ij}^2 \right|^{1/2}.$$

This is the optimal circulant preconditioner given by Chan[2] as:

$$c_i = n^{-1}(i t_{-(n-i)} + (n-i)t_i), \quad i = -(n-1),...,0,...,(n-1).$$

Now, except under very special conditions, the solution to the circulant system

$$Cx = b$$

will only approximate the solution to the equivalent Toeplitz system so some form of iteration is required. Many techniques such as preconditioned conjugate gradient, least squares and various combinations are available but, with a view to optical processing, a simple linear iteration was chosen. That is, for the system

$$Tx = b$$

we solve

$$Cx_{n+1} = (C - T)x_n + b.$$

At each step, there is a circulant inversion and a Toeplitz multiplication, both of which, as we have seen, can be achieved by calculation of a Fourier transform or convolution. This sequence will converge if the eigenvalues of $C^{-1}T$ are close to unity or, equivalently, if T is well conditioned, i.e., if $\|T\|\|T\|^{-1}$ is small. Such an iteration can be continued until the desired degree of accuracy is achieved.

If the covariance matrix is rectangular or block Toeplitz, equivalent results can be obtained as can be seen from the following argument. Following Ref. 3, suppose T is an m x n matrix. By extending the Toeplitz structure of T and, if necessary, adding zeros, we can assume that m = kn for some integer k. So we can consider kn x n matrices of the form

$$T = \begin{pmatrix} T_1 \\ T_2 \\ \vdots \\ T_k \end{pmatrix}$$

where each square block T_j is a Toeplitz matrix. If T is a rectangular Toeplitz matrix, then each T_j must be Toeplitz[3].

As in Refs. 4 and 6, for each block T_j, we construct a circulant approximation C_j in the manner described above. Then the preconditioner is a square circulant matrix C given by

$$C = \sum_{j=1}^{k} C_j * C_j.$$

Each C_j is an n x n circulant matrix. Hence, as we have seen, they can all be diagonalized by the Fourier transform matrix F, viz.,

$$C_j = F\Lambda_j F^*$$

where Λ_j is diagonal[2]. Thus the spectrum of the C_j can be computed by a Fourier transform. Since

$$C * C = F \sum_{j=1}^{k} (\Lambda_j * \Lambda) F,$$

C*C is also circulant and its spectrum can likewise be found by Fourier transform (optical or otherwise). Thus, we can choose[4,5]

$$C = F \left(\sum_{j=1}^{k} \Lambda_j * \Lambda \right)^{1/2} F *.$$

Regardless of the iterative algorithm chosen, improvement in performance can be obtained if, instead of the optimal circulant preconditioner described above, one chooses a so called "superoptimal" preconditioner defined to be the matrix C that minimizes

$$\left\| I - C^{-1} T \right\|_F$$

where I is the identity matrix. For an n x n matrix T, such a preconditioner can be achieved in O(nlogn) operations. (See, for example, Ref. 6 which discusses convergence criteria and offers comparisons to the Chan preconditioner[2].)

For certain important cases, such as in the presence of spatially correlated noise, the covariance matrix T can depart significantly from a Toeplitz structure. The technique of optimal (or superoptimal) circulant preconditioning can still be applied even if T is not Toeplitz or endowed with any special structure. In this case, a circulant preconditioner can be achieved in O(n²logn) operations[7]. Though this computation is much more expensive, it need not be carried out so frequently. Indeed, a single computation might be used as an input for several cycles of an iterative calculation. This will be significant when we discuss the optoelectronic implementation of these algorithms below.

A computer code, described in Section 2.1.1, was written to simulate the optical calculations of the Fourier transforms and convolutions required by this algorithm. At this point, it was becoming apparent that the advantages of a purely optical solution to this problem in the manner just described, although significant, were not compelling. Hence, a more general approach was initiated, incorporating some of the best features of the method described above and resulting in the optoelectronic architecture described in Section 2.2.

2.1.1 Computer Simulation of Toeplitz Inversion Algorithms

After arriving at a Fourier transform based algorithm for solution of linear systems, a computer code was developed in order to study a number of important issues such as convergence criteria, rates of convergence for iterative algorithms and susceptibility of this scheme to measurement and other types of errors. That simulation is described in this section. Although specific reference is made to Toeplitz systems, the same arguments apply to rectangular or block Toeplitz systems or non-Toeplitz systems where an optimal or superoptimal circulant preconditioner has been achieved.

Consider a Toeplitz system

$$Tx = b$$

where T is an n x n complex Toeplitz matrix and x and b a complex n vectors. Let C be a suitably chosen circulant matrix, say, optimal in the sense of Chan[2]. Consider the iteration

$$x_{n+1} = (I-C^{-1}T)x_n + C^{-1}b$$

where $x_n = 0$. This iteration converges in many instances and certainly in the case where any submultiplicative norm of $(I-C^{-1}T)$ is strictly less than unity. If x is the limit of this iteration, it is easy to verify that it is a solution to the Toeplitz system. This iteration can be performed optically. Let F_k be the complex discrete Fourier transform operation on vectors of length k. We recall that if C is an n x n circulant matrix and z is an n vector then Cz is just the cyclic convolution of the first column of C with z. Hence,

$$Cz = n^{1/2} F_n^{-1}(F_n c \bullet F_n z)$$

where c is the first column of C and

$$(x_1,...,x_n) \bullet (y_1,...,y_n) = (x_1 y_1,...,x_n y_n).$$

All these operations can be performed optically.

If z is an n vector, then

$$y = C^{-1}z$$

can be easily computed since

$$Cy = z$$

and, so,

$$F_n c \bullet F_n y = F_n z$$

provided that each component of Fnc is not zero.

Now, if T is an n x n Toeplitz matrix, let C(T) be the 2n x 2n circulant matrix created from T in the manner of Section 2.1. We will call C(T) the *circulant extension* of T. If $x = (x_1,...,x_n)$ is an n vector, we define a 2n vector $E(x) = (x_1,...,x_n,0,...,0)$. We will call E the *extension operator*. If $y = (y_1,...,y_n,y_{n+1},...,y_{2n})$ is a 2n vector, we define $T(y) = (y_1,...,y_n)$. We will call T the *truncation operator*.

We see that

$$Tx = T(C(T)E(x)).$$

Hence, Tx can be computed easily from the simple E and T operators plus F_{2n} applied to c(T) and $E(x)$. All this can be achieved by optical means.

The formulation just described was cast in C code. It was put to limited use because, as has already been mentioned, the more general optoelectronic architecture described below, seemed more appealing.

2.2 Optoelectronic Architectures for Solution of Linear Systems

The problem addressed here is to solve for the adaptive steering vector of an antenna array to steer a beam in azimuth-Doppler space with clutter and interference nulled. Given are the non-adaptive steering vector and a sample covariance matrix of the clutter and interference. The equation to be solved is

$$\mathbf{R}\vec{\mathbf{x}} = \vec{\mathbf{b}} \tag{1}$$

where:

$\vec{\mathbf{b}}$ = the non-adaptive steering vector to point the array to a location in azimuth-Doppler space,

$\mathbf{R}$ = the sample covariance matrix of clutter and interference,

$\vec{\mathbf{x}}$ = the adaptive steering vector to point the beam in the desired direction in azimuth-Doppler space with clutter and interference nulled.

An optical processing approach is considered here to iteratively solve Equation (1) for $\vec{\mathbf{x}}$.

In order for the iteration to be stable, and to speed the rate of convergence, the covariance matrix is preconditioned. That is, both sides of Equation (1) are pre-multiplied by an approximation to the inverse of the covariance matrix:

$$\mathbf{G}^{-1}\mathbf{R}\vec{\mathbf{x}} = \mathbf{G}^{-1}\vec{\mathbf{b}} \tag{2}$$

where

$\mathbf{G^{-1}}$ = is the approximate inverse of the sample covariance matrix $\mathbf{R^{-1}}$.

The Richardson algorithm is used here to iteratively solve Equation (2):

$$\vec{x}_{n+1} = \left(\mathbf{I} - \mathbf{G^{-1}R}\right)\vec{x}_n + \mathbf{G^{-1}}\vec{b} \tag{3}$$

where:

$\mathbf{I}$ = the identity matrix,

n = iteration step index.

The closer the approximate inverse matrix is to the inverse of the covariance matrix, the fewer the number of iterations required for Equation (3) to converge. Choices for the matrix $\mathbf{G}$, or its inverse, are:

$$\mathbf{G} = \mathbf{C},$$

where $\mathbf{C}$ is a circulant approximation to $\mathbf{R}$, easily obtainable when $\mathbf{R}$ is Toeplitz. $\mathbf{C}$ is also obtainable for $\mathbf{R}$ of more general form, but not as easily. The circulant matrix $\mathbf{C}$ is trivially inverted by a single Fourier transform. The procedure for obtaining a circulant approximation to R and inverting this circulant matrix is discussed in Section 2.1 of this document.

$$\mathbf{G^{-1}} = \mathbf{R_{old}^{-1}}$$

where $\mathbf{R_{old}^{-1}}$ is the inverse of a previous sample covariance matrix. This approach is applicable for the case that a large number of adaptive steering vectors are to be obtained covering a large area of Doppler-azimuth space. (Equation (3) can be iterated to solve for one column of the inverse of the sample covariance at a time by successively setting $\vec{b}$ equal to one column of the identity matrix.)

$$\mathbf{G^{-1}} = \mu \mathbf{I}$$

as a last resort, where $\mu < 2/\lambda_{max}$ and λ_{max} is the largest eigenvalue of $\mathbf{R}$. Since the sample covariance matrix is positive definite, the trace of $\mathbf{R}$ can be used as the upper bound on the largest eigenvalue of $\mathbf{R}$.

To streamline notation, Equation (3) is written as

$$\vec{x}_{n+1} = \mathbf{A}\vec{x}_n + \vec{h} \tag{4}$$

where

$$\mathbf{A} = \left(\mathbf{I} - \mathbf{G^{-1}R}\right)$$

$$\vec{h} = \mathbf{G^{-1}}\vec{b}.$$

9

The following two sections presents optical architectures to iterate Equation (4), a free space and two waveguide implementations.

2.2.1 Free Space Architecture

A free space architecture for iterating Equation (4) is shown in Figure 1. This architecture has been considered by a number of investigators[8, 9, 10].

In the architecture shown in Figure 1, the vector $\bar{x}_n$ can be represented by a linear array of LED's, laser diodes or point modulators. The reciprocal of the bandwidth of the $\bar{x}_n$ modulators must be less than or equal to the time it takes for the signal to make one round trip through the iteration feedback loop of the system. In principle, this could be on the order of 1 nanosecond, assuming a distance of less than 6 inches between the linear array and the detector array.

The matrix A is represented by a 2-D spatial light modulator (SLM). The update rate for A must be greater than or equal to the pulse repetition interval of the radar. The shortest typical pulse repetition intervals are on the order of 10's of microseconds. Some 2-D SLM's may operate at these speeds. An issue with this free space architecture, at least in past implementations, has been the limited dynamic range of 2-D spatial light modulators and, for STAP, potentially the limited framing rate. The performance of currently available SLM's is discussed below.

Laser Array or Modulator

SLM A

Detector array $A\underline{x}_n$

$\underline{x}_n$

$\oplus \underline{h}$

$\underline{x}_{n+1}$

Iteration Feedback

proc_slm.cvs
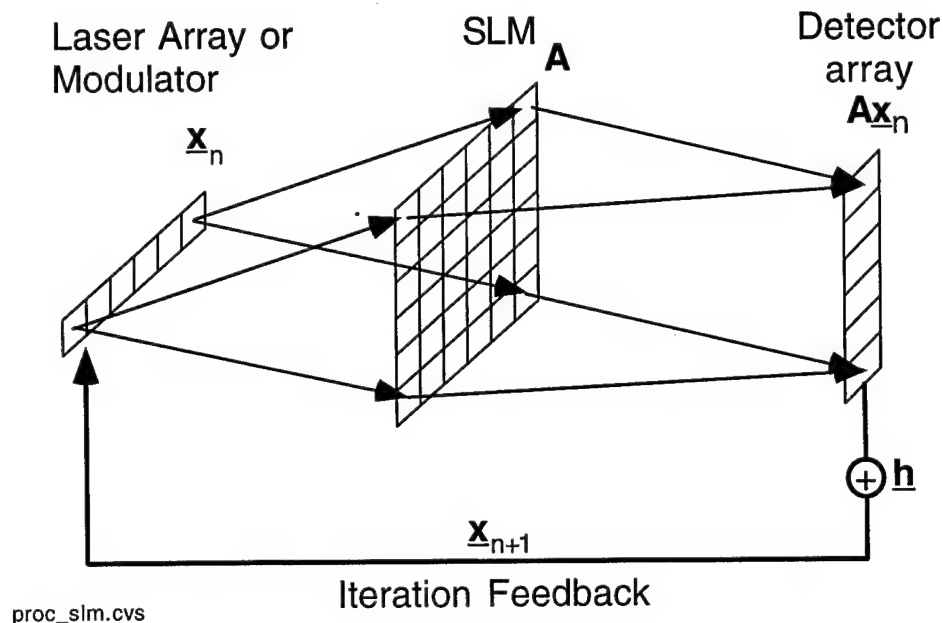
Figure 1: Free space optical architecture

10

2.2.2 *Optical Waveguide Architectures*

In order to overcome the current limits of 2-D SLM's, optical waveguide architectures are also considered. Compared with the free space architecture, the waveguide approaches are inherently more stable and it is possible that the **A** modulation can be performed at a higher dynamic range. In a waveguide architecture, fast, high dynamic range waveguide modulators are used. Two categories of the optical waveguide architecture are presented here, one in which the optical representation of $\bar{x}$ precedes the representation of matrix **A** and the other in which the $\bar{x}$ modulation follows that of **A**.

The representation of an analog optical waveguide processor to iterate Equation (4) in which the $\bar{x}$ modulation precedes the optical representation of **A** is shown in Figure 2. As in the architecture shown in Figure 1, the vector can be represented by a linear array of LED's, laser diodes or point modulators. The light representing the value from each of the elements of $\bar{x}_n$ is split into N unique paths where each path is then amplitude modulated. This imprints the values of the matrix **A** on the optical beams. This effectively multiplies an element of $\bar{x}$ times each element in the appropriate column of **A**.
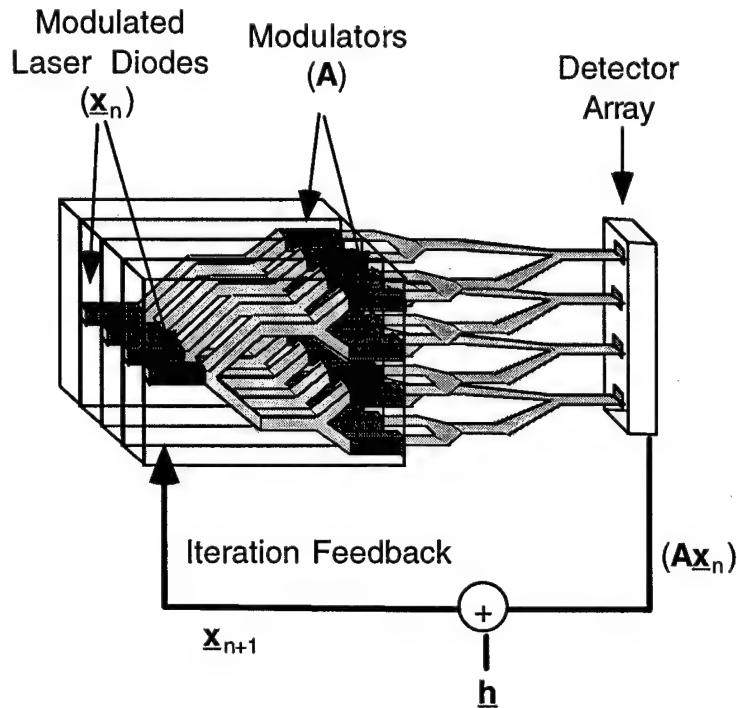
stack3.cvs

Figure 2: Optical waveguide architecture with vector $\bar{x}$ before matrix **A**

11

As shown in Figure 2, the N different optical paths from a row of **A** are combined and directed to an element of a photodetector array. The output of the detector array contains the results of the matrix-vector product, $A\bar{x}$. This result is then summed electronically with $\bar{h}$ to obtain the next step in the iteration for $\bar{x}$. This result is the iterative feedback that is used to drive the modulators for $\bar{x}$. The iteration is complete when $\bar{x}$ has converged to the desired value.

The representation of an analog optical waveguide processor to iterate Equation (4) in which $\bar{x}$ follows the optical representation of **A** is shown in Figure 3. This approach admits a less expensive method for **A** modulation (direct modulation of laser diodes) and a potentially shorter iteration loop than the waveguide architecture shown in Figure 2. In the architecture shown in Figure 3, light at N different wavelengths is split into N unique paths where each path is then amplitude modulated. This imprints the values of the elements of **A** on the optical carriers.
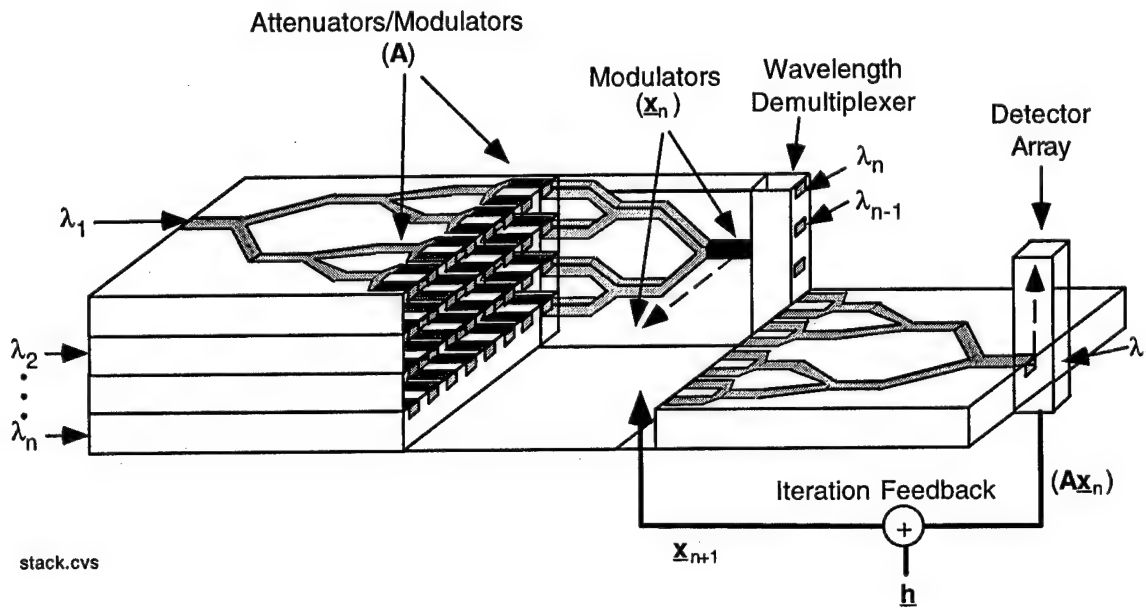
Figure 3: Optical waveguide architecture with vector $\bar{x}$ following matrix **A**

As shown in Figure 4, the N different wavelength channels for a column of **A** are combined and amplitude modulated. This effectively multiplies an element of $\bar{x}$ times each element in the appropriate column of **A**. As shown in Figure 3, a set of wavelength demultiplexers are used to separate the results of these multiplications. The crosstalk between channels in the demultiplexer will limit the precision of the processor. However, by adding narrow bandpass filters prior to detection, the crosstalk can be significantly reduced at the cost of a small amount of additional loop delay.

$\underline{\mathbf{h}}_j$

$(\mathbf{A}\,\underline{\mathbf{x}}^{(n-1)})_j$

$\underline{\mathbf{x}}_j^{(n)}$

+

From
Detector

$\mathbf{A}_{i,j}(\lambda_i)$

$\mathbf{A}_{i+1,j}(\lambda_{i+1})$

$\Sigma_i \mathbf{A}_{i,j}(\lambda_i)\underline{\mathbf{x}}_j^{(n)}$

To Wavelength
Demultiplexer

superscript: iteration loop index
subscript: element(s) of vector (array)

eo_mod.cvs
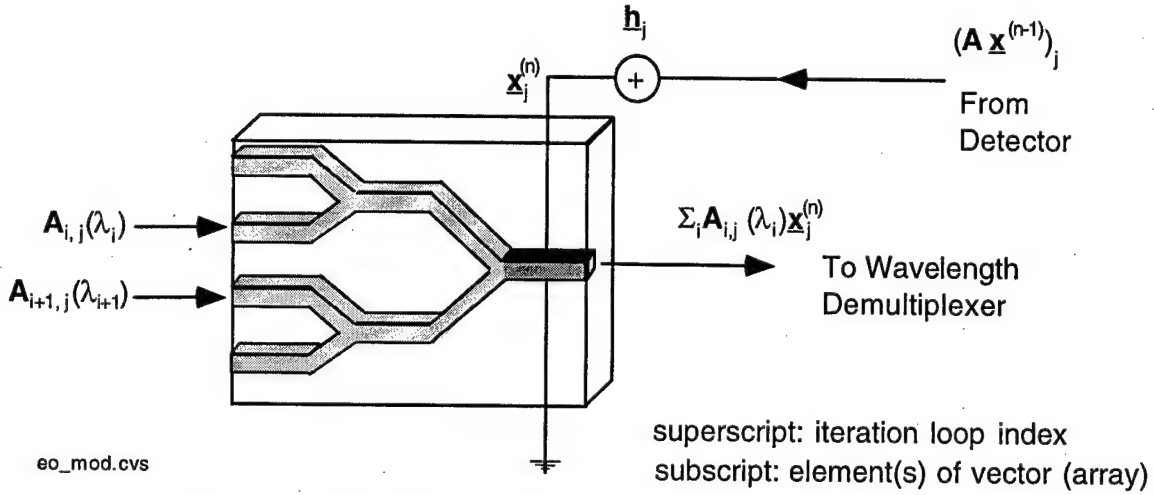
Figure 4: Schematic of operation of the waveguide approach

Optical signals of the same wavelength are then recombined and summed incoherently on a detector of the array of photodiodes. When a single optical source is used for each wavelength, the desired incoherent summing on the detector is obtained by insuring that the differences in the path lengths from each of the wavelength sources to the corresponding detector array element is greater than the coherence length of the source and that the line width of the optical sources are broader than the bandwidth of the photodiodes. Incoherent summing can also be obtained if independent mutually incoherent sources of sufficiently broad bandwidth are used for each element of $\mathbf{A}$. This approach is shown in Figure 4.

As in the $\vec{\mathbf{x}}$ first architecture, the output of the detector array will contain the results of the product $\mathbf{A}\vec{\mathbf{x}}$ and this result is summed electronically with $\vec{\mathbf{h}}$ to obtain the next step in the iteration for $\vec{\mathbf{x}}$.

Various different components and schemes can be used which will change the appearance of the architecture shown in Figure 3, but the operation of the processor will remain the same.

The main difference between all the designs lies in their method for achieving an optical representation of $\mathbf{A}$. The architecture shown in Figure 3 uses a single laser diode (LD) at each wavelength and splits each guide into N paths. The values of the matrix are then loaded by externally modulating the light in each path with an amplitude modulator. This design has the advantage of requiring only N LD's. The update time for $\mathbf{A}$ is estimated to be within 50 ns to 1 ms so the external modulators will require speeds of only 1-20 MHz which can be easily achieved.

Since the modulation speed for the $\mathbf{A}$ values is rather low compared with GHz rates for communications, direct modulation of the LD's can be performed. In addition to allowing

13

for direct modulation, the approach of using N^2 LD's would readily provide larger optical powers resulting in higher resolution for the processor.

An approach using N LD's on a single substrate, with each LD emitting at a distinct and evenly spaced wavelength is depicted in Figure 5. Direct modulation of each LD imprints the values of a column vector of **A** on the emitted light. The optical paths on the substrate are combined and directed into an amplitude modulator which would perform the multiplication with an element of $\bar{x}$. By repeating this module N times, the complete matrix - vector multiplication is accomplished. This design, which offers sufficient optical power, ease of implementation and compactness is the preferred design.

awaveg.cvs
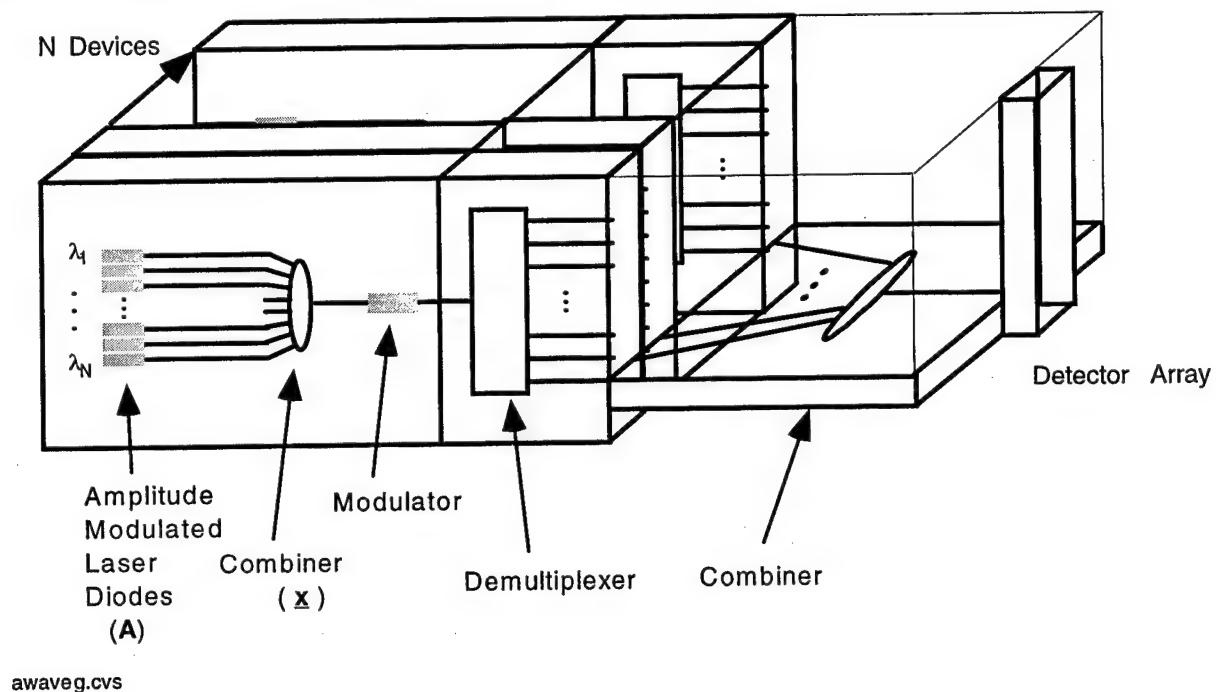
Figure 5: Preferred implementation of waveguide architecture with $\bar{x}$ following **A**

2.2.3 Comparison of the Optical Architectures

Additional information and analyses are required in order to select which of the above architectures to implement. The goal is to maximize computational speed and accuracy while minimizing size, weight, power consumption and cost. Complicating the trades between the three architectures presented is the fact that the trades should be based on anticipated capabilities and costs of technologies at the time such a processor would be fielded, which could be several years away. Much of the relevant technology is enjoying rapid development and, in some cases, rapid reductions in cost. The optical waveguide approaches rely on emerging technologies in the communications industry where the quality of devices is rapidly improving and the associated costs dropping.

In the following, the relative strengths and weaknesses of the architectures considered are summarized. The architecture that depends on the use of WDM technology appears to be the most complex. However, this architecture allows for an optimal match between modulator costs and inherent capabilities and required performance. An array of modulated laser diodes can be used to input the A matrix since the modulation bandwidth is low. That is, the amplitude level of the laser diode is changed only from one radar pulse to the next, i.e., when A is updated. In this architecture, the high speed $\bar{x}$ modulators are waveguide modulators. For the waveguide architecture with $\bar{x}$ first, it may not be appropriate to represent $\bar{x}$ by modulating the laser diodes if high enough performance, in terms of dynamic range and speed, can not be obtained with directly modulated laser diodes.

Additional factors to be considered in the trade off studies are summarized in the table below.

| | Free Space | Waveguide Architectures | |
		A matrix first	x vector first
x modulation	Modulated LD array	EO modulators	Modulated LD array
A modulation	2-D SLM	Modulated LD array	EO modulators, semi-conductors, optical amplifiers
Advantages	No WDM, No combiner losses	Modulation technologies ideally match requirements, technology being launched for optical communication	No WDM, potential for eliminating combiner losses, technology being launched for optical communication
Disadvantages	Limited dynamic range of 2-D SLM's, not as rugged as waveguide architectures	Requires WDM, combiner losses, WDM currently limited to 64 channels	Not ideal match of modulation techniques to requirements

Table 1: Architecture Issues/Trades

2.2.4 Optical STAP with Photonic Controlled Array

An architecture which directly integrates the optical STAP with a photonic controlled array is depicted in Figure 6. The solution for the adaptive steering vector would be performed as discussed above. In this figure, which is appropriate only if a single optical module could be used to compute the steering vector (in fact, 8 running in parallel are required when the matrix and vector element values can be complex and positive or negative), the detection in the iterative loop is moved to the $\bar{x}$ modulators. The addition of $\bar{h}$ is effected by coupling

the output of an amplitude modulated laser diode into the return path to the modulator for $\bar{\mathbf{x}}$. In this way, the optical signals on the array of fibers represent the iterated adaptive steering vector and is carried, over the fiber, to the photonically controlled RF antenna. The iteration result, the adaptive steering vector, times the inputs $\bar{\mathbf{s}}$ from the antenna elements, also carried over optical fibers, would then be detected as the adaptively steered resultant $\bar{\mathbf{x}} \cdot \bar{\mathbf{s}}$.
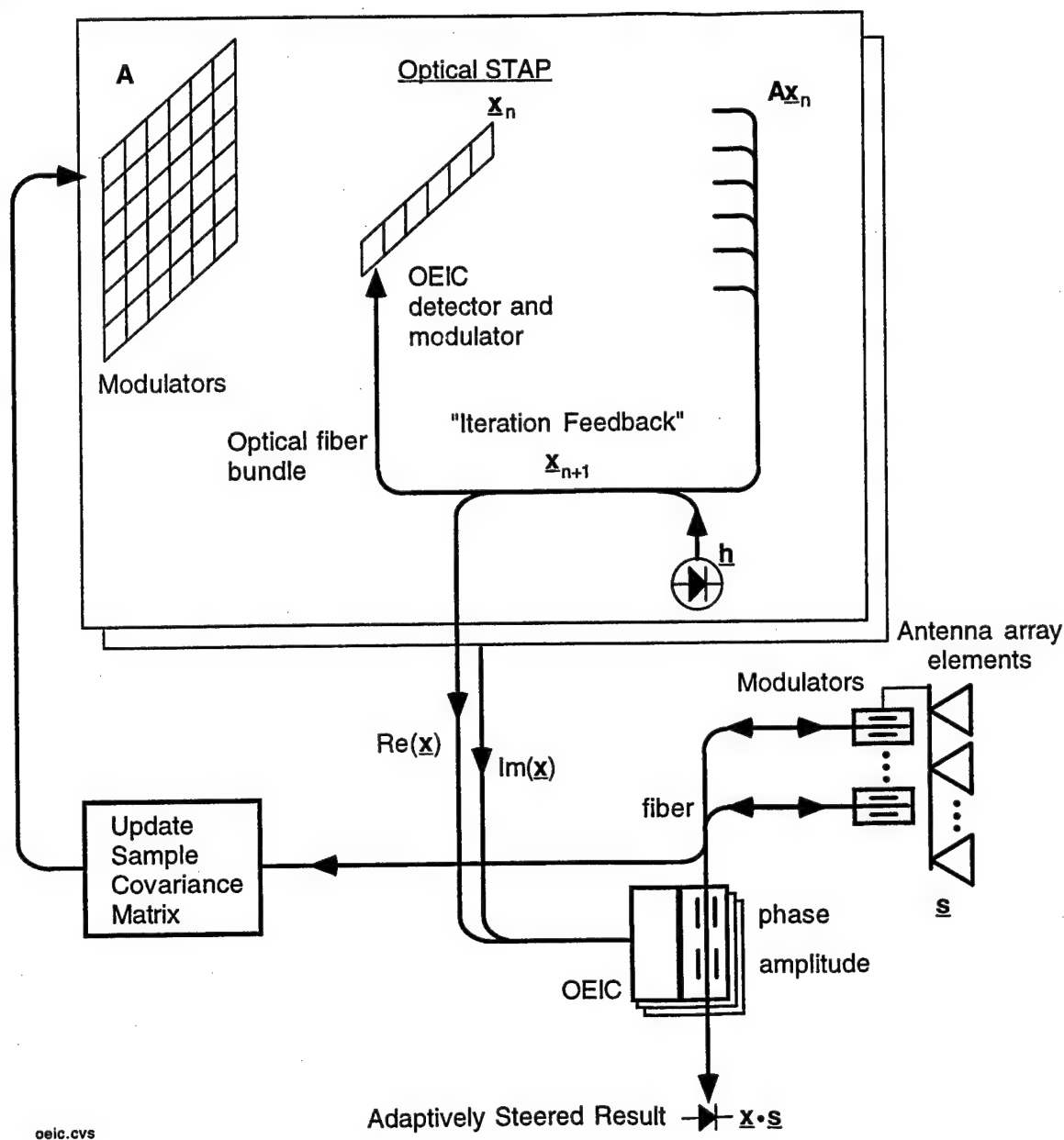
Figure 6: Integration of optical STAP in a photonic controlled antenna system

2.2.5 *Speed Advantage of Optical Architectures*

In this section the loop speeds of a digital and an optical STAP processor are compared. It is estimated that the loop speed of the optical processor is more than an order of magnitude faster than a digital processor. The comparison is given in terms of loop iteration period.

2.2.5.1 Digital Processor Array Architecture

Figure 7 displays the architecture for an array of digital processors to perform the matrix-vector multiplication and addition required to iteratively solve the equation,

$$\vec{x}_{n+1} = A\vec{x}_n + \vec{h}.$$

In this section, the time to perform the computations on an idealized digital array processor for one loop of the iteration is estimated.
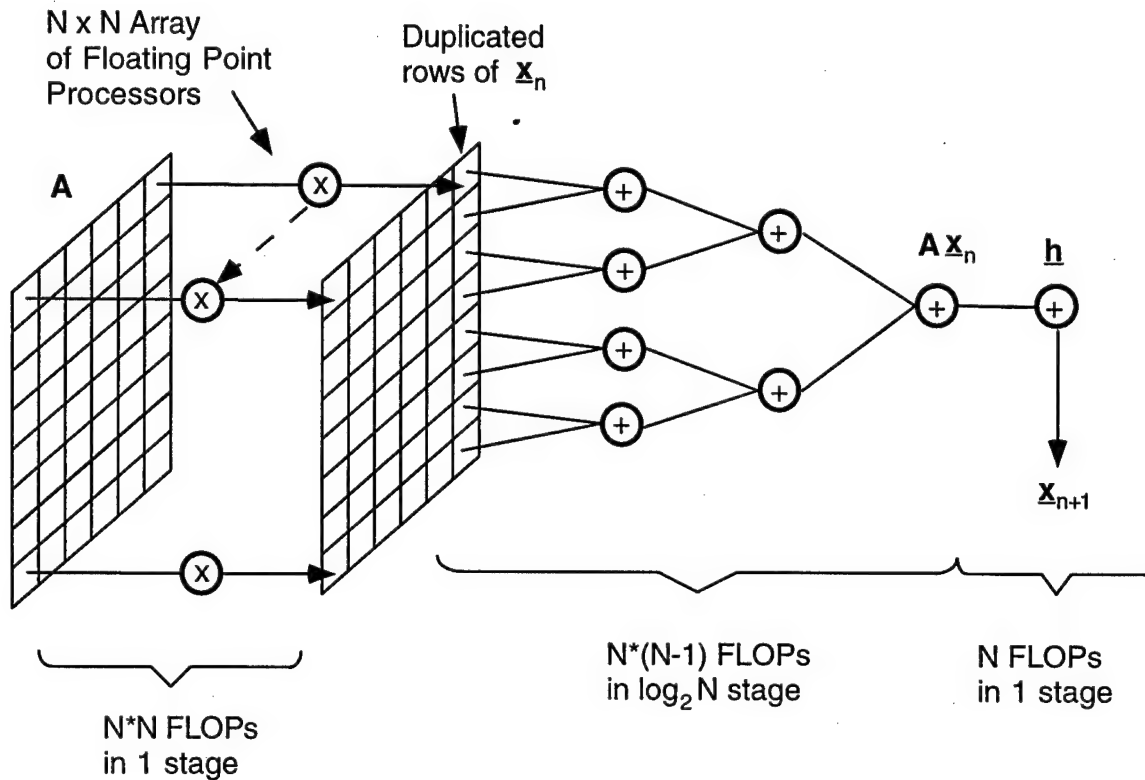
Figure 7: STAP digital array processor architecture

To perform, in parallel, the matrix-vector multiplication of **A,** a square matrix of dimension N, times a vector $\vec{x}$ of length N requires an array of N by N processors. The summation of the product terms are performed in a binary tree architecture and requires $\log_2 N$ stages. This summation requires $N^2/2$ processors for the first stage of the tree and may reuse some of the

original N^2 processors used in the multiplication. The addition of the vector $\bar{\mathbf{h}}$ requires only one stage and N processors. Thus there are $\log_2 N + 2$ stages in the iteration loop.

It is assumed here that the steady state sustained speed of each processor is 60 MFLOPs. This steady state sustained processing rate is used in the estimate here which corresponds to a processing time for each stage of 16.7 ns. Multiplying this value times the number of stages required per iteration loop provides an estimate of the loop iteration time. For example, an 8x8 matrix requires 5 stages which would take 83.5 ns. Loop periods for a number of array sizes appear in the table following the discussion of the speed of the optical architecture.

2.2.5.2 Optical Architecture

The iteration loop period for an optical waveguide STAP processor is proportional to the path length of the loop, which involves both optical and electrical connections. It is assumed here that an optical path length of approximately 6 inches should be realizable for a 64x64 or smaller array. Based upon an index of refraction of 1.5 for the waveguide architectures, this corresponds to an optical transit time under 1 ns. Assuming an equivalent time for the electronic path, an iteration loop period of 2 ns is used for estimating the speed of an optical processor for 64x64 and smaller matrices. This same estimate is used for both of the waveguide architectures and for the free space architecture. As noted above, the addition of a narrow band transmission filter to decrease channel crosstalk in the second optical waveguide architecture would increase the loop period by a small amount. As discussed below, this path length increase for the optical filters should be under 5 cm and therefore would add less than 0.3 ns to the loop period.

With larger matrices, the optical path length will increase, resulting in an increased loop period. By examining the increase in the dimensions of the combiner in the waveguide architectures, the increase in the loop period can be estimated. Given that a 64 to 1 coupler is achievable within a 6 cm long device, a matrix size of 1024, which requires 8 of these couplers, can certainly be realized in under a foot which will add less than 2 ns to the loop period. The same increase in loop period is assumed for the free space architecture as the size of the array becomes larger. The table in the following section contains estimates of loop periods for the optical architecture as a function of matrix size.

2.2.5.3 Comparison of Optical and Digital Architectures

From estimates in Table 2, the optical calculation is approximately 50 times faster than the digital one for 16 by 16 and larger matrices. So if the solution for a 256 x 256 requires 500 iterations, the digital processor requires 83.5 msec to obtain a solution while the optical processor requires only 1.5 msec.

Matrix Size (N)	Loop period (ns)	
	Digital	Optical
8	83.5	2
16	100.2	2
256	167.0	3
1024	200.4	4

Table 2: Estimate of loop period versus array matrix size for digital and optical array processors

The estimates for the loop periods for the optical calculation with larger matrices are conservative. With an efficient design, these may become smaller and the optical method may scale with the size of the matrix more slowly than the digital array approach which is proportional to the $\log_2 N$. Thus for larger matrices, there may be an additional benefit to be realized with the optical approach.

2.2.6 Complex and Negative Matrices and Vectors

The optical processors described above are limited to positive real valued operation. However, by linking multiple modules as shown in Figure 8, the solution of complex valued matrices and vectors can be obtained. Each box, representing a matrix vector product, requires one of the processors shown in Figures 1, 2, or 3. The additions are performed electronically.

realimag.cvs
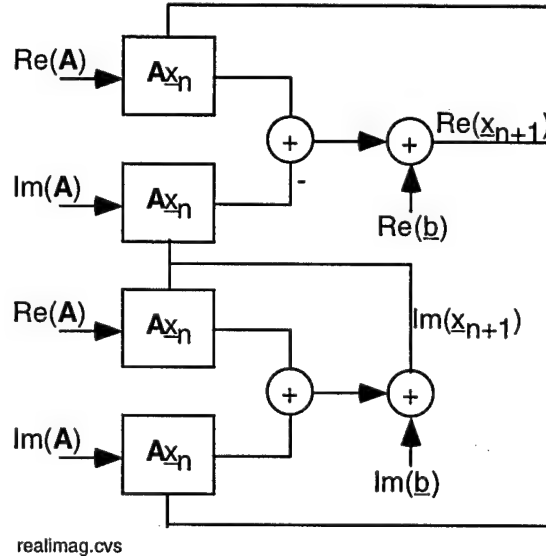
Figure 8: Solution for the complex valued matrix-vector iteration

Since the optical processor detects optical power, negative values are not admissible with a single optical module. However, by adding biases to $\mathbf{A}$, $\vec{x}$ and $\vec{h}$, we can develop a system with multiple optical modules to handle negative values. Select a matrix $\mathbf{D}$ which, when added to $\mathbf{A}$, yields a positive matrix $\mathbf{A}'$. Likewise, a vector $\vec{d}$ can be chosen which, when added to $\vec{x}$, yields a positive vector $\vec{x}\,'$. From Equation (4) we have,

$$\vec{x}_{n+1} + \vec{d} = (\mathbf{A} + \mathbf{D})(\vec{x}_n + \vec{d}) + \vec{h} + \vec{d} - \mathbf{D}(\vec{x}_n + \vec{d}) - (\mathbf{A} + \mathbf{D})\vec{d}, \tag{5}$$

which can be rewritten as

$$\vec{x}'_{n+1} = \mathbf{A}'\vec{x}'_n + (\vec{h} + \vec{d} - \mathbf{A}'\vec{d}) - \mathbf{D}\vec{x}'_n. \tag{6}$$

Equation (6) can be represented as in Figure 9 where the output of each module is now positive.
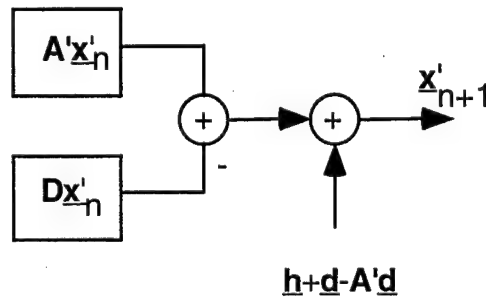
Figure 9: Method for handling negative values

The implementation of a complete complex valued optical processor would appear as in Figure 8 where each module is replaced by the $\mathbf{A}'\vec{x}\,'$ - $\mathbf{D}\vec{x}\,'$ pair of modules and the addition of $\vec{h}$ is replaced with $\vec{h} + \vec{d}$-$\mathbf{A}'\vec{d}$.

2.2.7 Obtaining Desired Accuracy

To obtain the desired accuracy from a limited accuracy processor, the solution can be divided into a series of limited precision parts. The quantities $\mathbf{A}$, $\vec{x}$ and $\vec{b}$ are expanded as,

$$\vec{x}_n = \vec{x}_n^{(0)} + 2^{-m}\vec{x}_n^{(1)} + 2^{-2m}\vec{x}_n^{(2)} + \ldots$$
$$\vec{h} = \vec{h}^{(0)} + 2^{-m}\vec{h}^{(1)} + 2^{-2m}\vec{h}^{(2)} + \ldots \tag{7}$$
$$\mathbf{A} = \mathbf{A}^{(0)} + 2^{-m}\mathbf{A}^{(1)} + 2^{-2m}\mathbf{A}^{(2)} + \ldots$$

where m indicates the number of bits of precision attainable and the superscript indicates the level of precision. When these expansions are inserted into Equation (4) and like precision terms are separated, the solution for the kth precision level of $\vec{x}$ is

$$\vec{x}_{n+1}^{(k)} = \mathbf{A}^{(0)}\vec{x}_n^{(k)} + \vec{h}^{(k)} + \sum_{m=1}^{k} \mathbf{A}^{(m)}\vec{x}_n^{(k-m)} \tag{8}$$

The overall iteration would start with the iteration for the most significant part (i.e. superscript of (0) and then continue through the lower significant parts. The summation term in Equation (8) would need to be computed only once per limited precision solution, and, therefore, can be computed digitally.

2.2.8 Method to Process Very Large Matrices

For the waveguide architecture using multiple wavelengths, shown in Figure 10, the number of different wavelength channels which can be used may be limited by the modulators or the wavelength demultiplexer. Fortunately, the waveguide concept can be expanded so that these limitations will not limit the size of the matrices which can be solved. In Figure 10 we show how modules with a limited number of channels can be linked. If p is the maximum number of wavelength channels that are attainable and, for example, the matrix size is $N = 2p$, a module of size p x $2p$ is built. Then, a second identical module is built which can reuse the same wavelengths or another spectral band. The output at the detectors of the two modules are concatenated to form the complete $A\bar{x}$ vector of length $2p$. This result is then fed back to both modulator arrays of length $2p$.

If the channel limitation is due solely to the limited spectral range of the modulators, an alternate architecture could be designed which uses wavelengths from λ_1 to λ_{2p} with a single set of wavelength demultiplexers (demultiplexing $2p$ channels) and a single detector array.
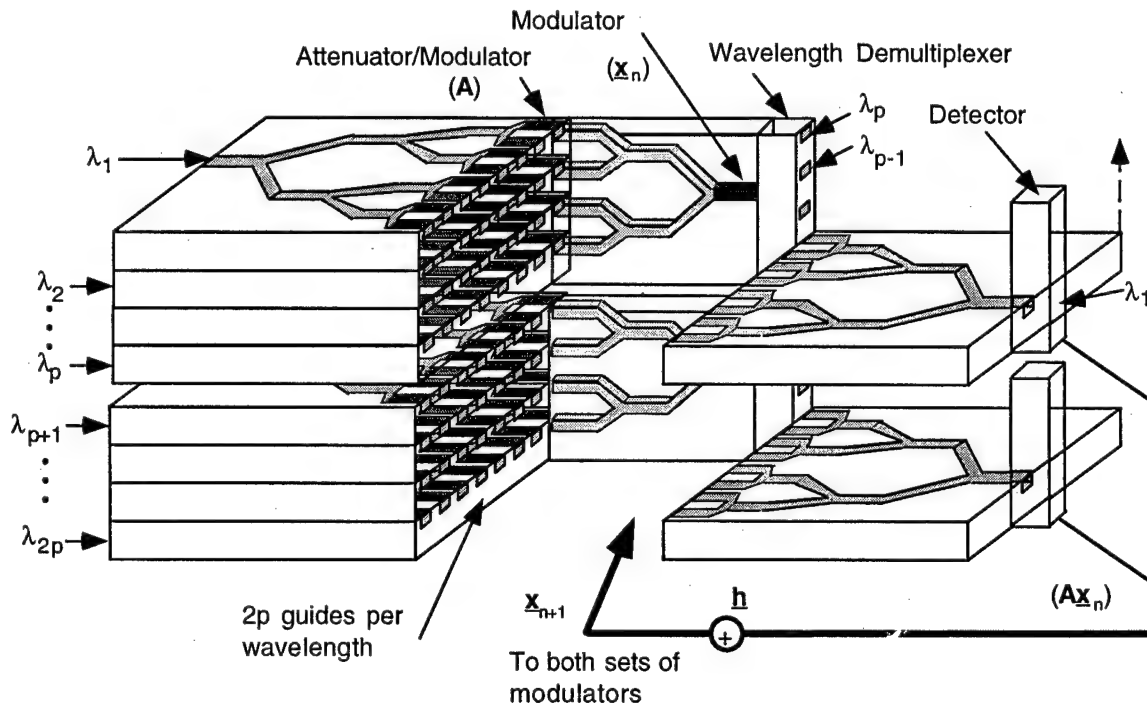
Figure 10: Optical waveguide architecture for large matrices

2.2.9 Simulations of Optical Architecture

The operation of the optical architecture was simulated using MATLAB. The goal was to test the convergence when multiple modules are used. In addition, variations in the detector bandwidth and loop periods were included to test operation for realistic component specifications. The effects of detector noise which is inherent in any optical system were included in the model. The simulations included various levels of channel crosstalk in the wavelength demultiplexers in the multi-wavelength wave guide architecture, or, equivalently, the cross talk between signals reaching the photodiodes in any of the three architectures considered. Using this simulation, the speed of convergence and the accuracy of the processor were estimated.

The simulation results in Figure 11 show the number of iterations or cycles required to find the adaptive steering vectors for two different covariance matrices as a function of the bandwidth - time (BT) product of the optical processor. In this case, the system was noiseless. The BT product is defined as the product of the loop period for a single iteration and the narrowest bandwidth of any of the components in the iteration loop. The results of this simulation indicate that the bandwidth should be at least the inverse of the loop period (e.g., 1 GHz for a loop period of 1 ns), and that there is negligible benefit in increasing the detector bandwidth beyond twice the inverse of the loop period.
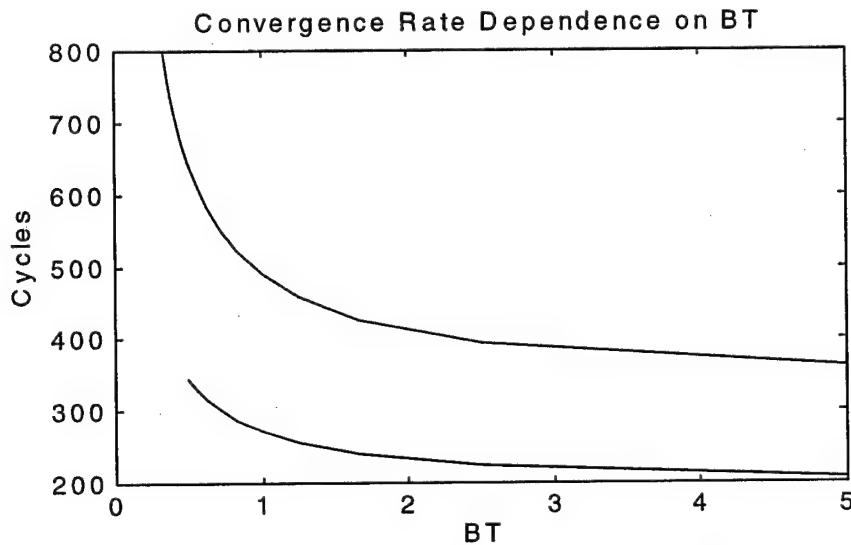
Figure 11: Number of iterations required for two different matrices versus the BT product in a noiseless system

In general, the form of the covariance matrix determines the likelihood of convergence and the number of iterations required for convergence. However, a good initial guess for the adaptive steering vector can dramatically decrease the number of iterations required to reach a solution. For the simulations represented in Figure 11, the elements of the initial steering vector were all zeros. However, in a real system where the covariance matrix is updated every pulse, using the last adaptive steering vector as the initial guess should dramatically decrease the number of iterations required since it is expected that the adaptive steering vector should change little from pulse to pulse.

In Figure 12, the convergence of the simulated system is demonstrated in terms of the relative error which is defined as the ratio of the magnitude of the difference between each iterated adaptive steering vector and the exact result to the magnitude of the exact result. In the following figures, the relative error as a function of cycle index is normalized to the relative error at the first cycle. The noise source in these simulations was assumed to be photon shot noise on the detector based on 10 μwatts of optical power incident on each detectors.
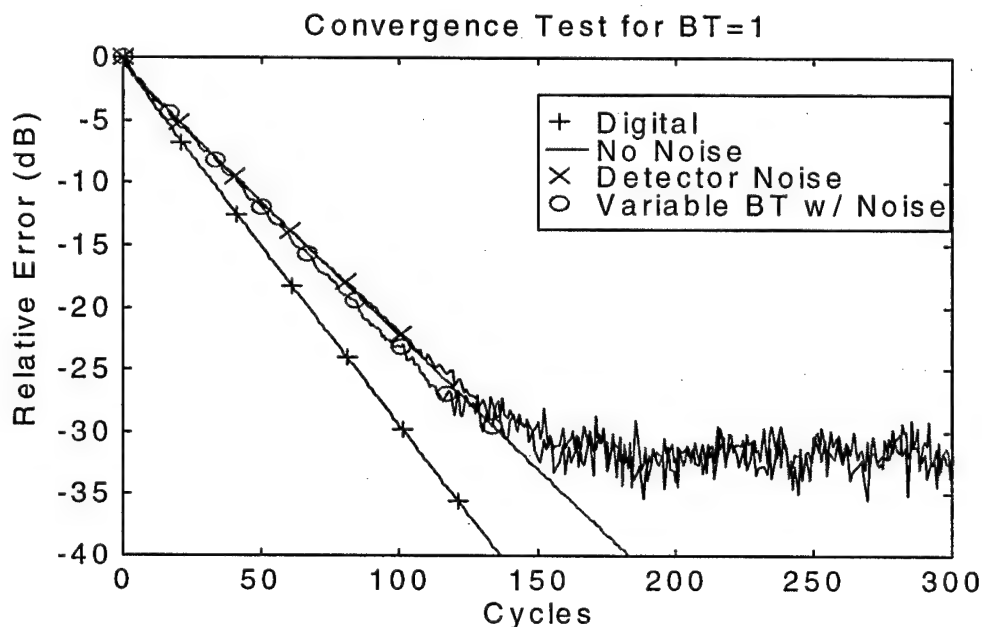
Figure 12: Error versus the iteration cycle index for a digital processor and for the optical processor with no noise and identical modules, with detector noise and identical modules, and with detector noise and a variance in the modules' BT

In this figure, the results for an 8 module processor which can handle complex covariance matrices and non-adaptive steering vectors are shown for a number of cases. First, the result with no detector noise and modules having identical loop periods and detector bandwidths

falls off linearly on a logarithmic scale. The cases with detector noise and differences in the bandwidth and loop period from module to module also converge as rapidly until a noise floor is reached. In these cases, the results were accurate to about 10 bits. As previously discussed, improved precision can be achieved by individually solving for the limited precision parts. Also, the effect of matrices having a range of condition numbers on the rate of convergence and on the noise floor needs to be determined. From Reference 11 it is expected that the level of the noise floor will vary in a near linear way with condition number of the matrix. In order to obtain a reasonable rate of convergence and low noise floor, the input matrix is preconditioned, as indicated above.

The rate of convergence of the iteration using a simulation of a digital array processor is also shown in Figure 12. These results, and an estimate of the loop period for a digital array processor, will permit a direct comparison with the proposed optical processor. Convergence rate of the optical processor is seen to be faster than the digital processor. This is expected because the BT products of the optical processor modules are approximately 1, rather than 2 or greater. The analysis of the digital array architecture necessary to solve the iteration showed that $\log_2 N + 2$ FLOP stages were required. Recall that the loop period of a digital processor for a 4x4 matrix is 67 ns. When this is compared with the achievable 2 ns loop period for the optical processor, it becomes apparent that the optical processor can offer a substantial improvement. For the vector solution in Figure 12, the digital calculation required 100 iterations and the optical one approximately 150 iterations to reach an error of - 32 dB. Therefore the digital array processor would require 6.7 μs to converge while the optical processor would converge in only 0.3 μs.

Since channel crosstalk, i.e., cross talk between the signals going to the different detectors, may limit the precision of the processor, its effects in the system were simulated to determine the maximum allowable level. Of particular concern is the cross talk in the wavelength demultiplexer in the multi-wavelength waveguide architecture. In Figure 13, the relative error is plotted verses the number of cycles with varying degrees of channel crosstalk. For the -20 and -30 dB crosstalk levels, the solution was limited to -15 and -25 dB in the relative error, respectively. However, with -40 dB crosstalk, the result converged to the detector noise limited -32 dB level. Results similar to those in Figure 12 are, of course, dependent on the form of the matrix solved. However, from other simulations, a channel crosstalk level of -40 dB also appeared to be satisfactory for the result to converge to the level of the detector noise. As mentioned above, if the WDM demultiplexer cannot provide this level of crosstalk, narrow band transmission filters can be inserted prior to detection.

Effect of Crosstalk with BT=1
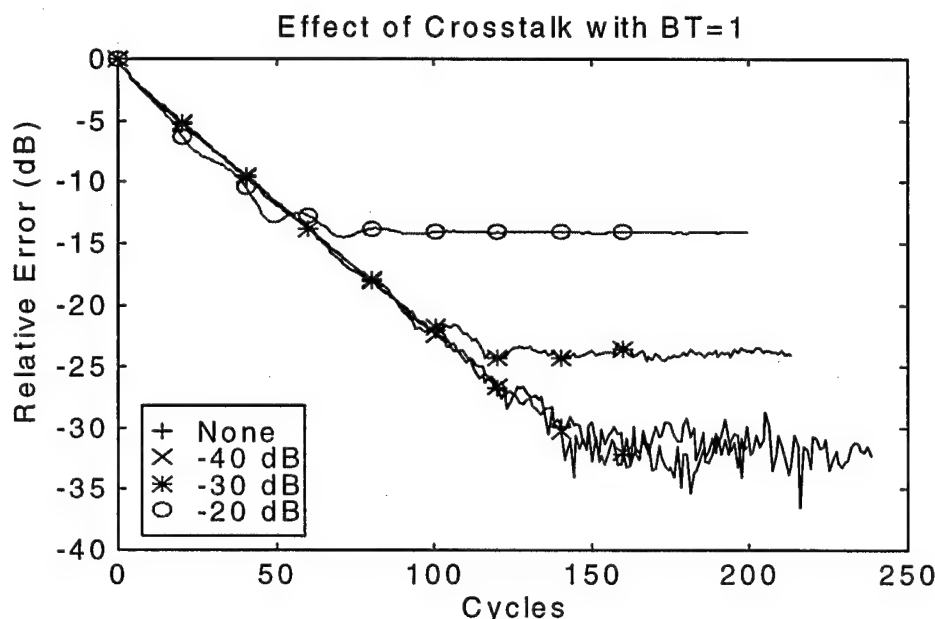
Figure 13: Relative error in the adaptive vector versus iteration cycle index for several levels of channel crosstalk in the WDM demultiplexer

In summary, the desired BT product should be between 1 and 2, the system continues to work properly with noise and relative scaling errors on the matrices and vectors between the multiple channels, though these errors decrease the number of significant bits of the solution. Finally, in order to maintain the detector noise limited resolution, the channel crosstalk must be limited to approximately -40 dB or less.

2.2.10 Implementation

Each of the analog optical processors considered for STAP processing requires a subset of the following components: laser diodes, 2-D spatial light modulators (SLM's), optical waveguides, amplitude modulators, wavelength demultiplexers, photoreceivers and waveguide star couplers and splitters. Except for the SLM's, these devices have been developed for the telecommunications industry and the device quality is rapidly improving to meet the increasing demands. In the following sections, the requirements of the components will be explained and the device technologies meeting these requirements will be discussed. Various technologies can be used for each of the components which changes the appearance of the architectures described above. The following discussion is based on components designed for 1.3 and 1.55 mm operation for the waveguide approaches and at a wavelength such as 680 or 830 nm for the free space architecture.

•

2.2.10.1 Planar Waveguide Coupling

One of the key issues in the waveguide approach is the manner in which light is coupled from one device to another. As shown in Figure 5, the desired devices would be integrated on planar light wave circuits (PLC). Butt coupling between two PLC's is more attractive than pigtailing and connecting fibers for reasons of compactness and lower insertion loss. However, this introduces the issue of accuracy in the channel waveguide pattern processes. Since the channel waveguides can be very narrow (5 μm for single mode guides), the accuracy of the channel waveguide location must be on the order of a micron or less. In conversations with silicon waveguide manufacturers, we have learned that accuracies on the order of 1 μm can be achieved in waveguide patterns. In addition, they have recently begun studying butt coupling two PLC chips.[12] However, as shown in the design in Figures 2 and 3, we would prefer to stack multiple PLC's on top of one another and butt couple to another PLC stack which has been rotated by 90 degrees. This would impose the same micron tolerance on the thickness of the silicon wafer which could not be achieved. However, using multi-mode guides would allow for a greater tolerance in the waveguide locations. These type of alignment issues will be considered further before a final architecture is chosen.

2.2.10.2 Light Sources and Modulation

The most straight forward approach for inputting the values of the $\bar{x}$ vector or A matrix, depending on which comes first in the architecture, is to directly modulate an array of laser diodes, one diode per element of the vector or array. As indicated above, the optical architectures assume amplitude only modulation. Therefore, it is required that the individual beams coming from each of these modulated input sources be mutually incoherent at a detector. This can be assured if mutually incoherent optical sources are used for each of the inputs and the line width of each of the lasers is wider than the detector bandwidth. Given that the bandwidth of the detectors is 2 GHz, LD's with a spectral bandwidth greater than 12 GHz (e.g., 0.1 nm at 1.55 mm) will provide the incoherence. Commercially available DFB LD's with spectral bandwidths of 0.1 nm, can be directly modulated at multi GHz rates. If the required dynamic range (number of bits of resolution) using direct modulation can not be obtained at the high modulation rates, external modulation will be used. If, for external modulation, a single optical source feeds some number of modulators, the mutual incoherence can be obtained by incorporating path length differences between the paths from the LD to the modulators so that the light in the different paths is incoherent. For example, an LD with a spectral width of 12 GHz (0.1 nm at 1.55 mm) has a coherence length, λ_c, of 2.4 cm in free space. Therefore, incoherence can be achieved by creating waveguide patterns where the path length, Δl, differs by more than 2.4 cm between any two routes. Figure 14 depicts the manner in which this could easily be achieved.

Delay $\Delta l > l_c$

Laser
Diode

Star
Coupler

Amplitude
Modulators

las_cohr.cvs
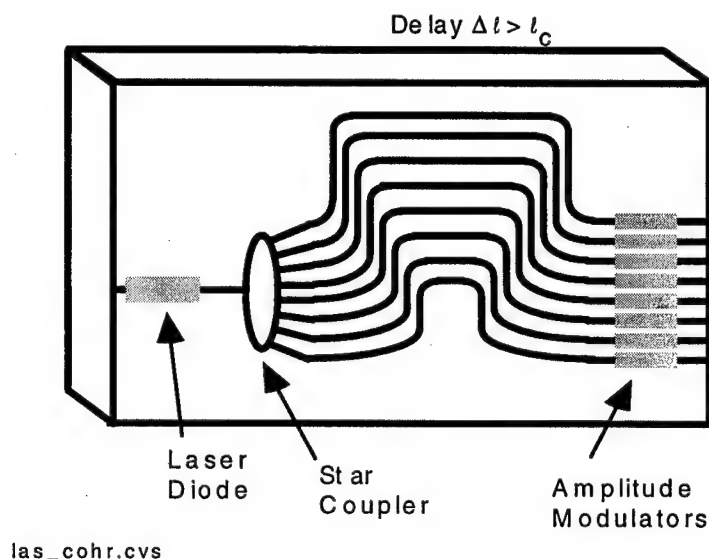
Figure 14: A scheme for implementing a single LD at each wavelength

Various forms of external modulation of the output of the LD's can be used to imprint the matrix **A**. Standard electro-optic (EO) amplitude modulators using a Mach-Zehnder design can operate at up to 18 GHz rates but are generally not monolithically integrated onto the same substrate as the LD. Electro-absorptive (EA) modulators are another external modulation scheme becoming increasingly popular for high speed (>10 GHz) modulation. These devices have been monolithically integrated with LD's on a single substrate for digital communication. Mitsubishi is currently marketing a 1550 nm distributed feedback (DFB) LD with a spectral line width of 12 GHz and an integrated EA modulator which can operate at 10 GHz.

Currently, indications are that direct modulation, in addition to offering the benefit of larger optical powers, is the least expensive method. Therefore, the preferred design shown in Figure 5 depicts direct modulation of N^2 LD's.

2.2.10.3 WDM Architecture Constraints on LD's

The path lengths through the device and the bandwidth of the detector place a limit on the narrowness of the laser spectral bandwidth. However, with the desire to process larger matrices, more wavelength channels are necessary and the channels must be placed closer together. Thus, the laser spectral bandwidth must also be balanced with the trade off of the fineness of channel separations as well as the acceptable crosstalk between channels.

In addition, custom orders for emission at specific wavelengths are routinely supplied for WDM applications.

Operational systems will implement many channels to solve large matrix-vector iterations. This will require many LD's with densely packed wavelengths and narrow lines. The use of monolithic wavelength division multiplexing (WDM) laser arrays which have multiple lasers operating at evenly spaced wavelengths is an attractive option for achieving the desired wavelengths for a lower cost than single lasers on each substrate. As shown in Figure 5, the matrix **A** is generated by N such devices operating at N wavelengths with each individual LD being directly modulated.

Such devices are already being developed for the telecommunications industry. A group at Bellcore through DARPA funding for the Optical Network Technology Consortium (ONTC) has produced a device with 10 wavelengths which are evenly spaced by 2 nm with an accuracy of 0.2 nm. [13] In this device, the output of the LD's are coupled and amplified by a semiconductor optical amplifier (SOA). The group has claimed production yields of around 80% which demonstrates the promising future of such a device. As shown in Figure 5, when the SOA in their device is replaced with an amplitude modulator, the first three stages shown in Figure 2 would be placed on a single substrate.

2.2.10.4 External Modulators

Depending on which of the optical processing architectures is implemented, and on its configuration, external modulators are used for either $\bar{x}$ or **A** or both.

If external modulation is used for $\bar{x}$ modulation, the quality of the amplitude modulator handling the feedback for the iterative $\bar{x}$ value is critical to the successful solution. Such a modulator must have a large dynamic range and requires linear modulation at high speed. In addition, based on the desired loop transit time of 2 ns, the modulation bandwidth of the device should approach 1 GHz.

The key issue for $\bar{x}$ modulator for the architecture using WDM's is the width of the spectral range which can be covered with linear operation of the modulators. This issue, and the wavelength demultiplexing channel separation limit, will effectively bound the number of channels and hence the size of the matrices which can be solved in a single module. It should be noted that variances in the linearity (i.e. different slopes of the amplitude modulation to applied voltage relationship) of the modulator for different wavelengths can be handled by tuning attenuators located in the waveguides before the detector or in the post detector electronics.

EO amplitude modulators satisfying the speed requirements and linear operation can be achieved when the device is biased to the quadrature level. Much work has been performed

to improve the linear operation and dynamic range of these devices. The geometry of the Mach-Zehnder limits operation to a given spectral range which depends on the desired tolerances in linearity. However, as a rough approximation, typical devices should exhibit approximately a 30-60 nm bandwidth over which the amplitude varies by less than 1%. The EA modulators are not based on an interferometer geometry, but they are limited to a certain spectral bandwidth where the optical transfer curve is linear. Current indications are that these curves are linear over a spectral bandwidth of less than 10 nm. Spectral range is important only in the architecture using WDM's.

Compelling arguments can be made for both devices. First indications show that EO modulators can be operated over a larger spectral bandwidth. EO modulators are typically linear to about 60% of the total modulation region which typically covers greater than 20 dB. EA modulators have a total modulation region of approximately 10 dB. Therefore, EO modulators will provide a larger dynamic range than current EA modulators. One argument in favor of EA modulators is that they are made from InGaAs and other type III-IV semiconductors which are easily integrated with LD's and should be less expensive than LiNbO$_3$ EO modulators. EA modulators also have lower capacitance and can be driven with less power but they currently suffer more than four times the insertion losses of EO modulators. Table 3 shows a comparison of the current EA and EO modulators.

Fermionics is in the final stages of developing EA modulators for the commercial market. They intend to have devices operating with bandwidths of 10 GHz on the market by the end of 1996 for an approximate cost of $1000.[14] This is already less than quality EO modulators. And it is expected that the cost of EA modulators would decline rapidly as the production quantities increase.

Characteristics	EO Modulators	EA Modulators
Supplier	IOC	Fermionics
Insertion Loss (dB)	3-4	10
Maximum Extinction Ratio (dB)	>20	10
Speed/Bandwidth (GHz)	2	10
Optical Bandwidth (nm)	50	<10
Driving Power (W)	<1	0.1-0.3
Capacitance (pF)	3-4	0.2

Table 3: Comparison of EO and EA modulators

The higher dynamic range and linearity of the EO modulators would increase the resolution of the solution and reduce the number of levels necessary for the complete solution. However, the implementation of several modulators on a single substrate would reduce the cost of the EA devices further. While EO modulators appear to be the only near term option, the progress in EA modulators will be closely watched to determine if they can replace EO modulators in future generations of the processor.

2.2.10.5 Two Dimensional Spatial Light Modulators

A 2-D (SLM) is shown in the free space architecture to represent the **A** matrix. The modulation required is amplitude only. SLM's are available from a number of vendors. For example, Boulder Nonlinear Systems, Inc. (BNS) manufactures a high quality 128x128 analog ferroelectric liquid crystal (FLC) reflective SLM. They have a 512x512 FLC SLM under development. The nominal frame rate of the 128x128 SLM is 1 kHz, and can be as high as 5 kHz. However, a significant fraction of the frame period is required for changing the state of the pixels (50 to 100 msec). In addition, for half of each frame period, the SLM is switched to its opposite state. Therefore, at a frame rate of 1 kHz, 300 msec of the 1 msec frame period is usable to look at data. When used in direct (zero order) back reflection mode, the dynamic range of this device is 70:1. In addition to the commercially available BNS SLM, others that may be available will be considered.

2.2.10.6 Wavelength Demultiplexing

For the architecture based on WDM's, the wavelength demultiplexer in the system is necessary to separate the results of the multiplication $\mathbf{A} \cdot \bar{\mathbf{x}}$. The issues driving the selection of the technology for wavelength demultiplexing include the center wavelength accuracy, channel or filter width, number of channels, crosstalk, insertion loss and cost. The tradeoff in the channel width would include the issues of crosstalk and the manufacturing accuracy and the stabilization for the center wavelength of the LD and WDM filters. If necessary, the alignment of the wavelength of the center wavelength of the LD with the WDM filters could be performed by temperature tuning the LD. Most of the LD and WDM demultiplexer devices have thermo-electric coolers to provide environmental stabilization.

The isolation (equivalent to the negative of the crosstalk) is a measure of the ratio of the power of the correct wavelength exiting a specified channel to the power of other wavelengths exiting the same channel. Low isolations will reduce the accuracy of the processor. In general, dense WDM demultiplexers exhibit slightly lower isolations between adjacent channels than the channels which are separated by more than the channel spacing. If the desired isolation cannot be obtained during the wavelength demultiplexing, a narrow band transmission filter can be added prior to each detector. This device would effectively remove light at any other wavelengths which, due to the limited isolation of the

demultiplexer, happened to enter this channel. Therefore, while locating the WDM device it will also be necessary to identify the need for and technologies available for these bandpass filters. In order to maintain a high resolution for the processor, the insertion loss of these devices should be kept small.

The estimated requirements for the wavelength demultiplexer in a demonstration system would include a channel spacing of approximately 1 nm. In order to prevent crosstalk between the channels, a channel width of 0.2 nm - 0.5 nm would be desired with an isolation of approximately 40 dB. In the following, some of the available WDM technologies are analyzed.

2.2.10.6.1 Dichroic or Dielectric Thin Film (DTF) Devices

In a dichroic or dielectric thin film (DTF) device, the filter structure is based on coating a glass substrate with alternating layers of slightly higher and lower dielectric materials with a thickness of one quarter or one half of the optical wavelength. This periodic index grating then selectively reflects light at a specified wavelength. Fabry-Perot cavities are fabricated from these gratings to serve as bandpass filters. In addition, multiple cavities are used to tailor the band shape to have flat tops and rapid falloffs.

Filters can be cascaded to realize multiple channel WDM devices. Usually, the filters are cascaded sequentially such that different channels experience different path lengths. In the design of our optical processor, this is a drawback because it causes different loop periods for the various spectral components of each element in the vector. This could be corrected by inserting various lengths of fiber on the output ports of the device. However a preferable option would be to use a nested or tree cascade structure which would keep the loop period short.

The following tables represent an example of the various devices commercially available using dichroic filters. While these devices are satisfactory for standard WDM systems with channel separations of larger than 1 nm, they cannot meet the requirements of dense WDM systems with channel separations of 0.1 nm - 1 nm. Therefore, these devices will be eliminated from further consideration.

Part Name	BWDM
Number of Channels	4
Channel Width(FWHM or 3dB)	3 nm
Channel Spacing	7.5 nm
Crosstalk	-25 dB
Excess Loss	1-3 dB
Temperature Dependence	0.02 nm/C
Cost	$4390

Table 4: ETEK wavelength demultiplexer using dichroic filters

Number of Channels	4
Channel Width(FWHM or 3dB)	< 1.1 nm
Channel Spacing	1.6 nm
Crosstalk	< -30 dB
Cost	$18,000-20,000

Table 5: Optical Corporation of America wavelength demultiplexer using dichroic filters

2.2.10.6.2 Grating-Littrow or Angularly Dispersive Devices

A number of different architectures are available which disperse wavelengths along different angles using gratings. Among these architectures are concave gratings or Rowland circle gratings which can be integrated into waveguides. In these devices, light from the input fiber is directed onto a concave grating mirror and then selectively reflected into one of many channels or guides. These devices can typically have a 1-4 nm channel separation but losses are generally in the 10-15 dB range.

Y. C. Chen's group at the University of Maryland Baltimore County (UMBC) has fabricated these devices using chemically assisted reactive ion beam etching.[15] They are currently developing demultiplexers and multiplexers for the Lightning Program which is involved in the development of a WDM network. In addition, under an DARPA funded project, Chen's group explored using these devices in a monolithic integrated WDM laser array.

Instruments S.A., Inc. has developed a similar grating device in which the light from the input fiber is directed onto a 3-D concave mirror and reflected onto a diffraction grating. The reflection from the diffraction grating routes the wavelengths onto individual fibers.

These devices can operate with single or multi-mode fiber and can have up to 131 channels with a channel spacing as small as 0.4 nm and very low polarization sensitivity.[16]

Part Name	Quote: Multi-Mode
Number of Channels	4/8
Channel Width(FWHM or 3dB)	0.2 nm
Channel Spacing	1 nm
Crosstalk	-30 to -55 dB
Excess Loss	<5 dB
Temperature Dependence	0.01 nm/C
Cost	$11,000/18,000

Table 6: ISA wavelength demultiplexer using diffraction grating

2.2.10.6.3 Array Waveguide Grating (AWG)

The array waveguide grating (AWG) or phase array waveguide grating (PAWG) incorporates two planar star couplers in SiO_2/Si or InP waveguides as shown in Figure 15. The input coupler directs light from each of the N channels into all of the N output ports of the first coupler. Each guide after the coupler is fabricated with a constant length difference between the neighboring guides. The phase differences which are created by the varied transmission lengths then steer the individual wavelengths onto one of the N output ports. When applied in the matrix-vector multiplication processor, this device would require only one input port.
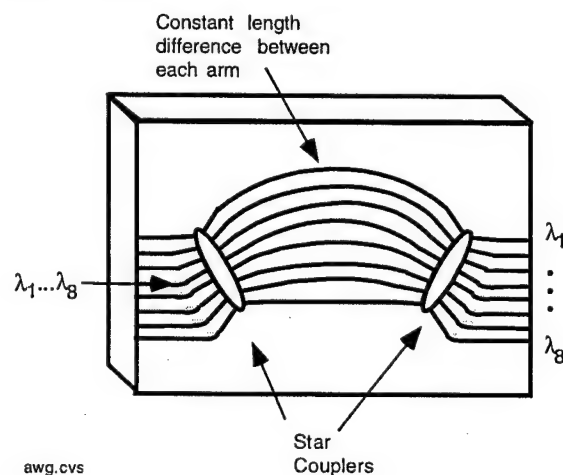
Figure 15: Layout of a typical array waveguide grating (AWG) wavelength demultiplexer

Typical AWG devices can achieve up to 64 channels with channel separations of 0.4 to 15, nm, isolations of 14-30 dB, insertion losses of 2-8 dB and low polarization sensitivities.[17] A group at AT&T have recently integrated one of these devices with a channel separation of 0.76 nm in a Terabit communications system.[18]

Number of Channels	32	64
Channel Width (FWHM or 3dB)	0.3 nm	-
Channel Spacing	0.8 nm	0.4 nm
Crosstalk	-28 dB	-27 dB
Excess Loss	2 dB	3 dB

Table 7: Typical Parameters for AWG wavelength demultiplexer (From Reference 17)

Y. C. Chen's group has also worked with these devices. They have developed the AWG masks and contracted Photonics Integrated Research Inc. (PIRI) to etch the AWG on silicon wafers. These devices exhibit very low loss and excellent performance. The accuracy for their device's center wavelength was approximately 0.2 nm and the accuracy of the channel separation was about 0.01 nm.[15] In addition, Chen states that the cost of a 10 channel unpackaged (i.e. not fiber pigtailed) device to be approximately a few thousand dollars for prototype quantities. As production quantities increase, he expects prices to reach several hundred dollars.

In a subsequent conversation with PIRI, it was found that they are currently manufacturing prototype quantities and claim accuracies of 0.1 nm for the center wavelength and 0.05 nm for the channel spacing. They have developed photomasks to build up to 32 channel WDM's with spacings as small as 0.8 nm. Their devices have also been integrated with thermo-electric coolers for thermal stabilization. For standard products the adjacent channel isolation is better than 22 dB and approximately 30 dB for the other channels. Table 8 shows the approximate costs of the currently available devices and prices are expected to decline by about 50% within the next year as quantities increase.

Number of Channels	4	32
Channel Spacing	0.8-1 nm	0.8-1 nm
Channel Width(FWHM or 3dB)	0.4 nm	0.4 nm
Insertion Loss	< 7dB	< 7 dB
Approximate Cost (packaged)	$7,000	$20,000
Approximate Cost (chip)	$3,500	$10,000

Table 8: PIRI wavelength demultiplexer[12] using AWG

2.2.10.6.4 Fiber Bragg Gratings

A group from the Communications Research Center (CRC) in Canada which have been researching Bragg gratings in fibers for a number of years, have developed another narrow band WDM device. The design shown in Figure 16 implements identical Bragg gratings which are written in two arms of a Mach-Zehnder Interferometer (MZI).[19] The light at the Bragg wavelength of the gratings reflects from the gratings and returns through the second arm of the fused coupler. The light at other wavelengths is transmitted through the gratings and exits the device through the second fused coupler. Though the two gratings are written simultaneously with a phase mask, there is a slight optical path length imbalance in the two arms.[20] This is corrected by what is referred to as "UV trimming". In this process, one arm is exposed to uniform UV light which increases the index and thus the optical path length, thereby balancing the interferometer.
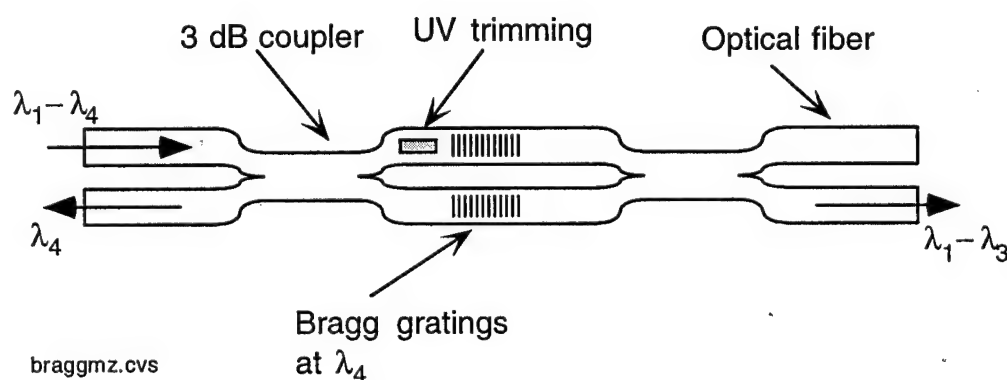
Figure 16: Mach Zehnder Bragg Grating Wavelength Demultiplexer

Number of Channels	NA
Channel Width(FWHM or 3dB)	0.2 nm
Channel Spacing	0.8 nm
Crosstalk	-20 dB
Excess Loss	0.5 dB
Temperature Dependence	0.015 nm/C

Table 9: CRC's Mach Zehnder Bragg grating wavelength demultiplexer[19]

Part of the group from the CRC formed a company called Innovative Fibers and are currently manufacturing a WDM device. Standard devices which are available have channel separations of 0.7 to 1.6 nm, channel widths of 0.1 to 0.5 nm, isolation of more than 20-35 dB

and insertion losses under 0.5 dB. In addition, Innovative Fibers have recently developed temperature control on the devices which reduces the wavelength shift with temperature to around 0.001 nm/C.[21] This is an important development and implies that more densely packed channels should be attainable.

Part Name	Quote: 4 MZI WDM Devices
Number of Channels	4
Channel Width(FWHM or 3dB)	0.5 nm
Channel Spacing	1 nm
Crosstalk	<-20 dB
Excess Loss	<2 dB
Temperature Dependence	0.01 nm/C
Cost	$10,750

Table 10: Innovative Fibers' Mach-Zehnder Bragg grating wavelength demultiplexer

The Bragg division(formerly known as Northern Photonics) of QPS Technologies is also developing fiber Bragg gratings for WDM devices.[22] They are currently producing prototype 4 and 8 channel devices with spacings of 1.6 nm with isolations of 30 dB (adjacent channel) and 35 dB (other channels).

These Bragg gratings could serve as the narrow bandpass filters required to increase the channel isolation. Under a previous contract, QPS has provided information on developing custom narrow channel (20 MHz) transmission filters.[23] Filters with a channel width of 0.4 nm, rejection of 25 dB and lengths under 5 cm can be easily obtained. The cost of these Bragg gratings has been decreasing rapidly over the past years as the production quantities have increased. Currently, standard gratings can be purchased for as little as 200 dollars each.

2.2.10.6.5 Bragg Gratings in PLC's

Another attractive option for demultiplexing is the use of the Bragg Gratings in planar light wave circuits (PLC). The CRC and NTT laboratories have been working on a device which uses Bragg gratings in silica based PLC's.[24] They have designed an asymmetric MZI which simultaneously demultiplexes three channels. The first channel is tapped in the same manner as the fiber WDM. The other two wavelengths are demultiplexed by the asymmetric length in the two arms of the interferometer following the gratings. They have installed heaters in the arms of the interferometer to balance the path length for the first channel and to provide the ability to alternate the ports where the other two wavelengths exit.

Number of Channels	3
Channel Width(FWHM or 3dB)	(1-2) & 4 nm (Estimates)
Channel Spacing	5 nm
Crosstalk	19 dB
Excess Loss	1.5 dB

Table 11: CRC's PLC Bragg grating wavelength demultiplexer[24]

Another group at AT&T Bell Labs have recently published results on a two channel demultiplexer which implemented bandpass filters written in P_2O_5 doped SiO_2 channel waveguides on silicon substrates.[25] Their device exhibited a 1.5 nm channel width and was claimed to be more stable to temperature effects. In addition they claimed that no UV trimming was necessary as in the fiber MZI to balance the interferometer.

2.2.10.6.6 Bragg Transmission Filters

Under the previous contract mentioned above, a channelizer for true time delay has been designed.[23] This device implemented fiber Bragg transmission gratings and was designed with channel spacings of 20 MHz or 0.2 pm.[26] The channelizer required substantial environmental stabilization and tuning control in order for the filters to transmit at the desired wavelength. The matrix-vector multiplication processor would probably never require such a fine channel spacing and thus the requirement for environmental stabilization would be reduced. For example, a spectral width of 50 nm with a channel spacing of 0.1 nm would allow 500 channels in a single module. While the benefit of using this device might be diminished by the added complexity of controlling and tuning, this approach is attractive and will be considered in further design analyses.

2.2.10.6.7 Wavelength Demultiplexing Summary

In summary, the 3D concave grating device, fiber Bragg gratings and the AWG demultiplexers will all meet near term requirements for channel spacing, number and channel widths. The isolation on the fiber Bragg grating demultiplexer and the AWG are below the desired 40 dB but the higher isolation demultiplexer for these devices could be custom designed. In addition, if the isolation requirement becomes too difficult or expensive to obtain, Bragg transmission gratings can be inserted in series after demultiplexing at a relatively low cost.

Of the three candidates for demultiplexing, the AWG seems to be the most affordable and to have the best design for integration in the optical waveguide processor. Future increases in the number of channels and the implementation of narrower widths in demultiplexers will require very environmentally stable operation. Fortunately WDM networks are currently in

high demand in the telecommunications industry and it is expected that the quality of these devices will continue to improve along with substantial price reductions.

2.2.10.7 Waveguide Combiners

Waveguide combiners are needed in the waveguide architectures. The only requirements for these combiners are that the guided modes are combined with minimal loss over a short distance. The combiner depicted in Figure 5 is actually a 1xN single mode splitter constructed of cascaded y-junctions in a silicon substrate which is operated in reverse. The unfortunate effect of using this device in reverse is that at each y-junction a 3 dB loss is incurred. Therefore, the optical power directed into one of the N input ports experiences a loss of at least $3*log_2N$ dB before reaching the output port. This loss will become unacceptable as N increases. While a large scale of this design will not be used, we have included the sizes of some unpackaged 1xN devices in the following table. Some alternate designs will be discussed below.

Device	1x16			1x32		
Size (mm)	length	width	height	length	width	height
	39	5.7	1.1	56.7	9.7	1.1

Table 12: Dimensions of unpackaged splitters available from PIRI[12]

Before turning to combiner designs, the requirements of the two different stages of combiners necessary in this processor will be discussed. The combiner prior to the modulation will direct the single mode waveguide output from the LD's into the electro-optic modulator and the AWG demultiplexer which operates with single mode guides. Therefore this combiner must have single mode inputs and outputs in order to mate with the LD's and demultiplexer. The second combiner stage will combine the single mode waveguide outputs of all the demultiplexers into a single path to the photodiode. Typical photodiodes which operate at GHz speeds have active areas of 75 μm and therefore can be pigtailed to multi-mode fiber. Thus, this combiner requires single mode inputs but can allow a multi-mode output guide. The relevance of this difference will become clear in what follows.

An alternate design for the combiner is depicted in Figure 17. This design would implement an Nx1 star coupler in a manner which is better illustrated in the figure. Such a device allows for keeping the length of the processor, and therefore iteration loop periods, short. The light incident from the N ports would be spread over the far side of the slab region where a portion would be collected by a larger single output port. If this output waveguide is tapered down to a small width corresponding to single mode, the loss for such a device is still expected to be $3*log_2N$ dB. It has not yet been determined if this loss can be substantially

reduced if the output waveguide is not tapered down to such a small width and the output remains multi-mode.

If the combiners precede the detector array, the output guide would not have to be tapered back to the width of a single mode but could remain up to 75 μm wide. An analysis can be performed to balance the reduction in optical loss of the combiner with the loss in bandwidth which occurs with further increases in the active detector area.

Single Mode Guides   Star Coupler   Taper Region   Multi-Mode Guide
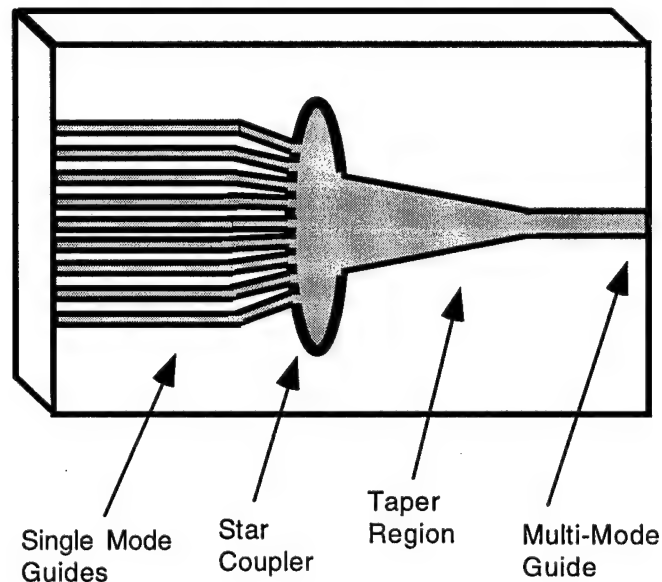
combiner.cvs

Figure 17: Proposed combiner implementing a Nx1 star coupler with taper

To avoid the large combiner losses in the waveguide architectures, the combiners before each of the detectors can be eliminated and the output ends of the waveguides imaged in free space on the photodiode array. Alternatively, each of the diodes can be replaced with a linear detector array of length N and the signals from N photodiodes at a time combined electrically. In this latter case, light from each of the waveguides, before any combining, is coupled into a photodiode. The losses incurred by combining in the electrical domain need to be determined.

2.2.10.8 Detection

The speed requirement of the photoreceiver can be determined from the simulations which showed that there is minimal gain in rate of convergence for increasing the time-bandwidth product beyond 2, where time is the loop period. For a minimum loop period of 2 ns, the desired minimum detector bandwidth is 1 GHz. Since this speed must be matched by the

post detector electronics, it is also desirable to have a transimpedance amplifier with a 50 Ω output impedance. Laser Diode Inc. manufactures a fiber coupled photoreceiver having the required transimpedance amplification that operates at 1 GHz at a cost of approximately $630 per device.

The requirements for future systems will probably not require higher bandwidth devices. However, better quality (i.e. higher sensitivity) devices will allow for increased resolution and thus possibly faster solutions. In addition, progress is being made on photodetector and photoreceiver arrays which could be implemented more compactly in the processor design.[27]

2.2.10.9 Post-Detector and Modulator Electronics

The electronics portion of the processor will amplify the detected signal, add the appropriate voltage for $\bar{h}$, drive the modulator array and perform the convergence test. A preliminary analysis indicates that the electrical amplification required is modest. If the range of optical power at the photodiode is 0.1 to 10 μW and the transimpedance gain for the receiver is 5 V/mW, the electrical signal before amplification will be 0.5 to 50 mV. To produce a 15 dB amplitude modulation, the transient voltage which must be applied to the modulator should be approximately 0 to 4 V. Therefore, a modest amplifier gain of approximately 80 is required. This analysis assumes that EO modulators are used for the $\bar{x}$ modulation.

2.2.11 Optoelectronic STAP Architecture Conclusions

Several highly promising alternative architectures exist for an efficient optoelectronic STAP processor. Although reasonably extensive, the current investigation of relevant device technology has not been exhaustive and further research is necessary to produce a definitive design. However, given the anticipated advantages over all-digital processors, such an effort is justified.

3. Task 2 - SAR Image Formation (SOW 4.1.2)

The purpose of this task was to establish the physical characteristics of image formation processors suitable for current and next generation SAR in order to compare all-digital and optoelectronic implementations with respect to size, weight and power consumption.

3.1 Digital Implementation

3.1.1 Algorithm Descriptions

Two basic SAR algorithms were considered in generating the sizing estimates discussed in this section. Algorithm A is based upon a polar algorithm and variants that are the basis of currently deployed image formation processing systems. The algorithm has been hosted on a

number of computing platforms employing both special and general purpose computing systems including MCS and Paragon equipment. Algorithm A differs from other implementations in the assumption that the geometric correction is applied to the complex data versus the detected image data and by the correction of algorithm induced phase errors. It can be shown that these differences result in only a slight increase in the size of the equipment.

A top level block diagram of the algorithm is shown in Figure 18. Important to the algorithm is the division of the radar supplied data into parallel channels of data, each representing data for an image segment at increasing range across the desired image swath. After the division of the input data, the processing is a direct implementation of the polar algorithm.

The primary advantage of this algorithm is that the division of the data into separate range segments can be accomplished using the filtering properties of the fast Fourier transform. Thus, the dividing of the image into subimages is accomplished using a computationally efficient signal processing technique. As a result, this algorithm reduces the computational capacity needed for implementation.

The primary disadvantage of this algorithm lies in the assumption that the target returns are represented by an ideal linear FM pulse. Amplitude and phase deviations from this ideal waveform reduce the quality of the imagery produced by the overall system. This type of error is known as a "spatially invariant" error and cannot be corrected using this algorithm. The quality of the imagery is highly dependent upon the high performance of the radar system.
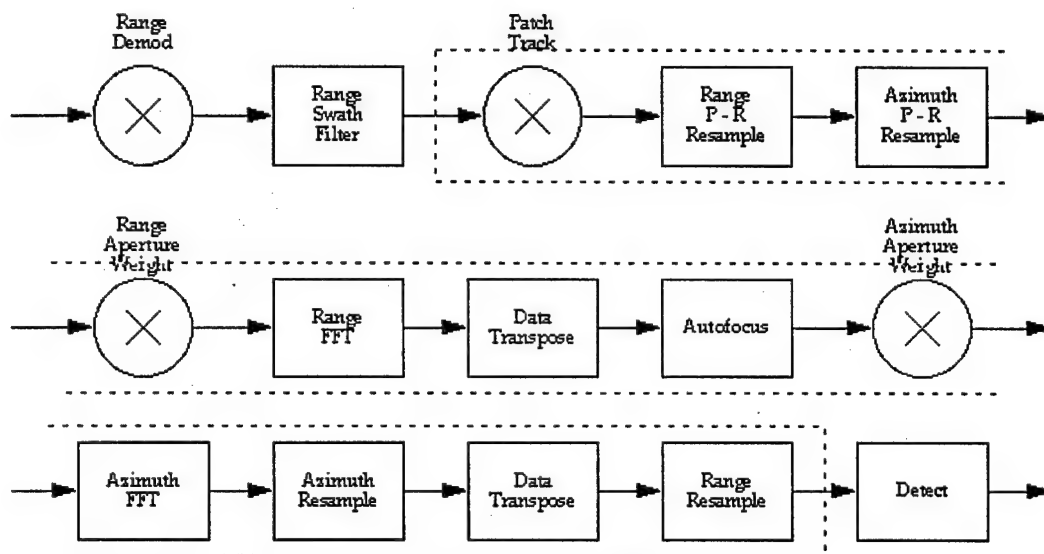
Figure 18: Top Level Block Diagram of Algorithm A

Algorithm B is also based upon the polar algorithm and its variants and likewise has been implemented on a number of host platforms. The typical implementation of Algorithm B includes a geometric correction applied to the complex data versus the detected image data and includes correction of algorithm induced phase errors.

Figure 19 shows a top level block diagram of the algorithm. The key feature and its primary advantage is the use of deconvolution to convert the incoming radar data into the desired frequency domain format. This algorithm is not dependent upon the waveform characteristics of the radar system to produce high quality imagery. Any radar waveform that provides adequate target illumination over a bandwidth suitable for the system range resolution can be employed.

The primary advantage of this algorithm is the ability to compensate for the class of distortions known as spatial invariant errors. As long as the amplitude and phase characteristics of the radar system are known, the algorithm can adjust the amplitude and phase to produce the ideal amplitude and phase data for polar processing.
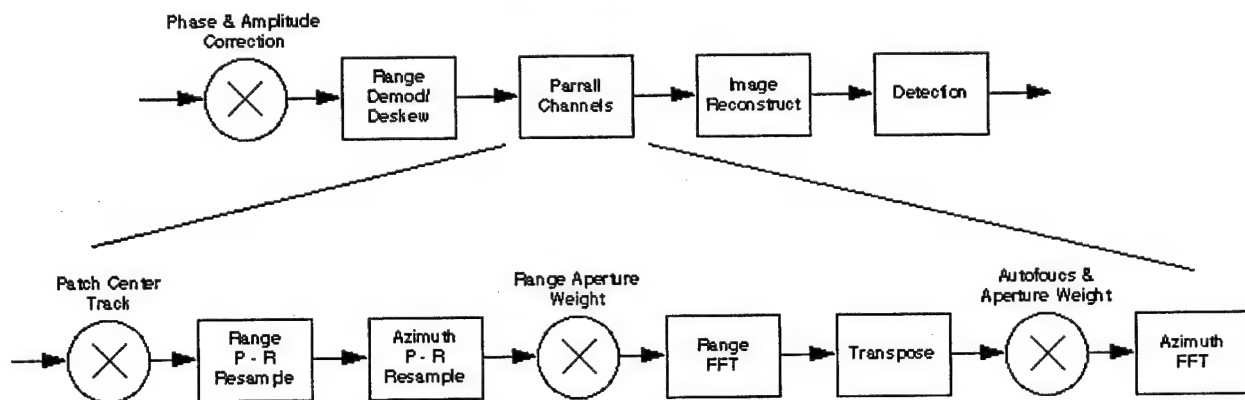
Figure 19: Top Level Block Diagram of Algorithm B

The primary disadvantage of this algorithm is the increased computational burden required. Specifically, the algorithm does not provide a computationally efficient mechanism to divide the incoming radar data into subimages for processing. (An exhaustive discussion of these two algorithms as well as the complete details of the methods employed in this analysis can be found in Reference 28.)

3.1.2 Radar Characteristics

The definition of the SAR systems for the analysis is key to both the optoelectronic and digital sizing analyses. It is the common origin for the size estimates and relates them to real world reconnaissance systems. This analysis is based upon two notional systems which is

representative of the expected performance for current and next generation SAR systems. The principal radar characteristics for these systems are summarized in Table 13.

	Current SAR	Next Generation SAR
Operating Range		
Minimum	20 nmi.	10 nmi. (20 km.)
Maximum	150 nmi.	110 nmi. (200 km.)
Range Coverage		
Swath Mode	10 nmi.	10.8 nmi. (20 km.)
Spot Mode	1 nmi.	1.08 nmi. (2 km.)
Azimuth Coverage		
Swath Mode	continuous	continuous
Spot Mode	1 nmi.	1.08 nmi. (2 km.)
Resolution		
Swath Mode	10 feet	3 feet (1 meter)
Spot Mode	3 feet	1 foot (0.3 meter)
Platform Velocity	700 fps.	590 fps. (650 knots)

Table 13: Top level performance characteristics for the SAR systems used in the sizing analysis

Both sets of characteristics are representative of SAR systems that are intended to provide standoff reconnaissance from a subsonic, high altitude aircraft. Both SAR systems are assumed to have two imaging modes, a swath mode to collect moderate resolution imagery covering large areas and a spot mode to collect high resolution imagery covering a limited patch area. The assumed platform velocities are representative of the average ground velocity of subsonic aircraft (the next generation system is based upon the velocity specification for the TIER II+ vehicle). The parameters for the next generation system are provided in both English and metric units since the TIER II+ system was specified in metric units.

The requirements provided in Table 13 are not adequate to define the parameters needed to specify the input data to the image formation processor (IFP). To define the data collected by the radar system and presented to the IFP requires the identification of certain radar characteristics which are provided in Table 14.

	Current SAR	Next Generation SAR
Nominal Wavelength	0.11 feet	0.11 feet
Transmit Pulse Length	100 μseconds	100 μseconds
Pulse Bandwidth		
Swath Mode	72.2 MHz.	222 MHz.
Spot Mode	241 MHz.	667 MHz.
Pulse Repetition Rate		
Swath Mode	450 Hz.	620 Hz.
Spot Mode	520 Hz.	520 Hz.
Antenna Az. Length	4 feet	2.6 feet
Samples per Vector		
Swath Mode	17764	57075
Spot Mode	3676	11093
Bits Per Sample (real/imaginary)	5/5	5/5

Table 14: Assumed radar system characteristics

Both radar configuration are assumed to operate at X-band and transmit a relatively long pulse. The transmitted pulse is assumed to be a linear FM with bandwidth adequate to support the final image resolution requirement. The radar pulse repetition frequency is selected to provide an acceptable azimuth ambiguity level for the specified antenna length and the vehicle velocity. Both radar systems are assumed to use a complex analog to digital conversion which has 5 bits for the real and imaginary portions of the sample. The number of samples per radar pulse or vector are shown in the table.

The parameters were selected to represent the expected characteristics for typical radar systems. The actual implementation of a given radar system can differ due to other design factors. However, the parameters given are consistent with the desired performance and can be considered as representative for the respective systems.

The final set of necessary definitions is the characteristics of the images produced by the IFP. There are two aspects of defining the image, the image vector produced by the system and the distortions and errors in the final image arising from the IFP. These definitions are given in Table 15.

The first row in Table 15 defines the size of the image vector produced by the IFP from the data supplied by the radar system. The errors and distortions in the image due to the IFP itself are described in the subsequent rows. Note that these rows define only the IFP

contributions to image quality and do not include errors due to the radar or other factors. It has been assumed that the primary image quality is determined by the quality of the data supplied to the IFP and that error contributions from the latter are relatively small. This assumption should not have a significant effect on the design and implementation of the IFP since the major sources of errors in the processor are deterministic and can be minimized or corrected using known design procedures.

	Current SAR	Next Generation SAR
Samples per Vector		
Swath Mode	8760	28880
Spot Mode	2992	8704
Geometric Distortion		
Absolute	< 1 sample	< 1 sample
Relative	< 0.1 sample	< 0.1 sample
Impulse Response	- 35 dB Taylor	- 35 dB Taylor
Multiplicative Noise Ratio	< - 18 dB	< - 18 dB
Noise Floor	< < radar noise floor	< < radar noise floor
Dynamic Range		
Swath Mode	> 80 dB	> 90 dB
Spot Mode	> 90 dB	> 100 dB

Table 15: Characteristics for the imagery produced

The image quality specifications define the allowable IFP errors associated with the geometric fidelity, the system impulse response and the radiometric fidelity of the image produced by the SAR system. Again, the listed errors and distortions are those introduced by the IFP and do not include those contributed by other portions of the system.

3.1.2.1 Results

The systems assumed in this analysis are based on the computer equipment produced by Mercury Computer Systems, using the i860 microprocessor and the computer modelling of that equipment described in Reference 28. Such systems are widely used in the SAR community and represent the equipment projected to be the platform for systems in the near future. This equipment has the hardware and software capacities to host the image formation processing for the class of reconnaissance system considered here.

The laboratory environment is considered to be any normal office environment, that is, where the ambient temperature and other factors are maintained for human comfort without special environmental conditioning for equipment.

The ruggedized environment refers to conditions where the operating environment is similar to an office environment, possibly with greater extremes, but includes a non-operating environment to allow the transportation of the equipment. This environment is typical for deployed ground equipment and certain airborne equipment.

The mil spec environment is, of course, that defined by Military Specifications for airborne electronic equipment.

	Algorithm A Current SAR	Algorithm A Next Generation SAR	Algorithm B Current SAR	Algorithm B Next Generation SAR
Laboratory				
Size (ft³)	7.0	7.0	7.0	7.0
Weight (lbs)	128	177.5	139	210.5
Power (watts)	928	1720	1104	2248
Ruggedized				
Size (ft³)	3.45	6.9	3.45	6.9
Weight (lbs)	117	267	129	300
Power (watts)	660	1760	820	2200
Mil-Spec				
Size (ft³)	1.32	2.64	1.32	3.96
Weight (lbs)	117	264	129	396
Power (watts)	600	1400	660	2100

Table 16: Physical characteristics of the equipment needed to implement digital IFP's

3.1.3 Optoelectronic Implementation

The *ImSyn*™ Processor makes it possible to carry out high speed image formation and complex valued correlation computations on inexpensive work stations. The patented system, which has recently entered commercial production, is based on an optoelectronic module that performs discrete two dimensional Fourier transforms. Originally conceived for the processing of SAR images, the processor can produce a variety of images, virtually independent of the sensor type[29].

The theory on which the *ImSyn*™ Processor is based is briefly described in Reference 29. The concept is to represent an object to be imaged as a set of Fourier components, scaled copies of which are measured as part of the sensing process. These scaled copies are summed, one frequency component at a time, and the inverse Fourier transform produces the image. Although, in some cases, such as radar imagery, the scattering process directly produces scaled copies of the spatial frequency components of the scene to be imaged, the same theory applies to cases where no scattering at all occurs but where wave-like mathematics obtains nevertheless. Thus, the *ImSyn*™ Processor is equally applicable, for example, to magnetic resonance imaging (MRI) where Fourier components are produced by the sinusoidally varying components of precessing proton spin vectors and x-ray tomography where the radiation can be represented as a Fourier series of spatially modulated x-ray intensities. Indeed, the mechanism by which the *ImSyn*™ Processor forms images is virtually independent of the sensing process.

The generalized architecture of the system is shown in Figure 20. The processor generates two mutually coherent laser beams, serving as the reference and sampling beams, which are focused at two points. Both beams are amplitude modulated by the square root of the measured amplitude of the return signal and the sampling beam is phase modulated by the measured phase of the return signal. The lens generates the two dimensional Fourier transform of the two beams on a time integrating photodetector placed on the focal plane of the lens. The transform is represented by an interference pattern, the spatial components of which are illustrated in Figure 20. By moving the spots with their varying relative phase, the full set of scaled Fourier components of the object to be imaged can be created with amplitude and phase corresponding to the measurement for that component.
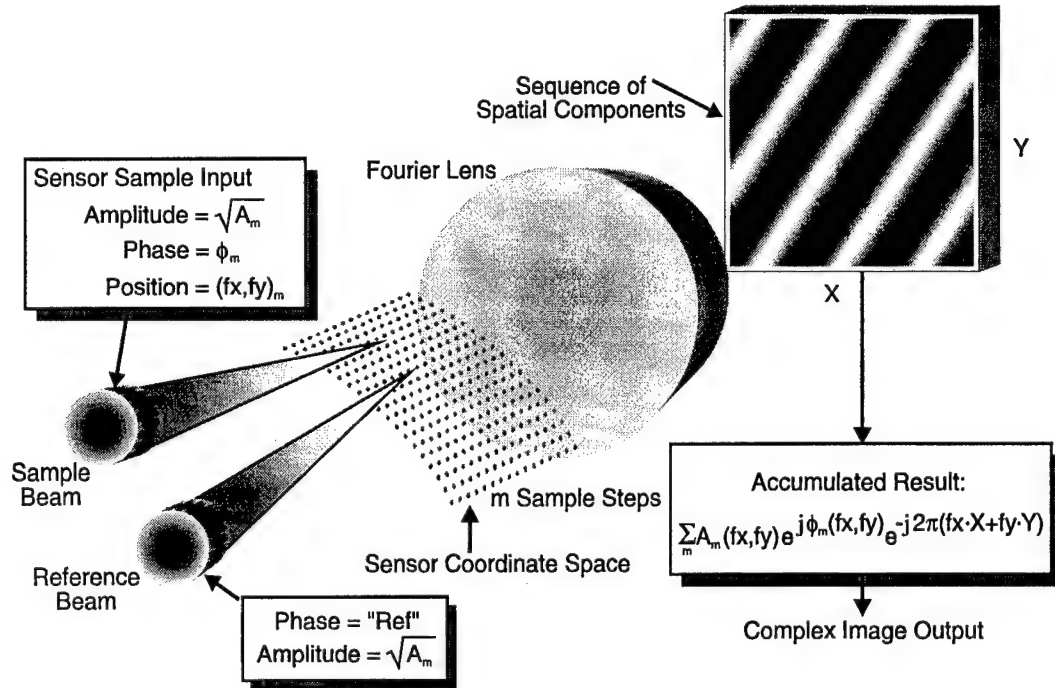
Figure 20: *ImSyn*™ Processor Architecture

Acousto-optic deflectors (Bragg cells) are responsible for moving the spots. The Bragg cells are driven by a digital frequency synthesizer whose waveform depends on the geometry of the frequency space sampled. The high precision with which the spots can be located and the fact that the interference pattern contains all the phase and amplitude information about the object to be imaged account for the ability of the *ImSyn*^{TM} Processor to transform data sets even from non-uniformly sampled frequency spaces of arbitrary geometry, without coordinate transformations or interpolations.

The photodetector integrates the complete set of spatial frequency components, at which point an accumulation buffer contains the complete complex image represented by that set of frequencies. The real and imaginary parts of the complex data are processed separately and amplitude, power and phase can be displayed. Processor controls permit selection of integration times and the orientation and scaling of the image resulting from the data.

A functional block diagram of the Essex *ImSyn*™ SAR Processor is shown in Figure 21.
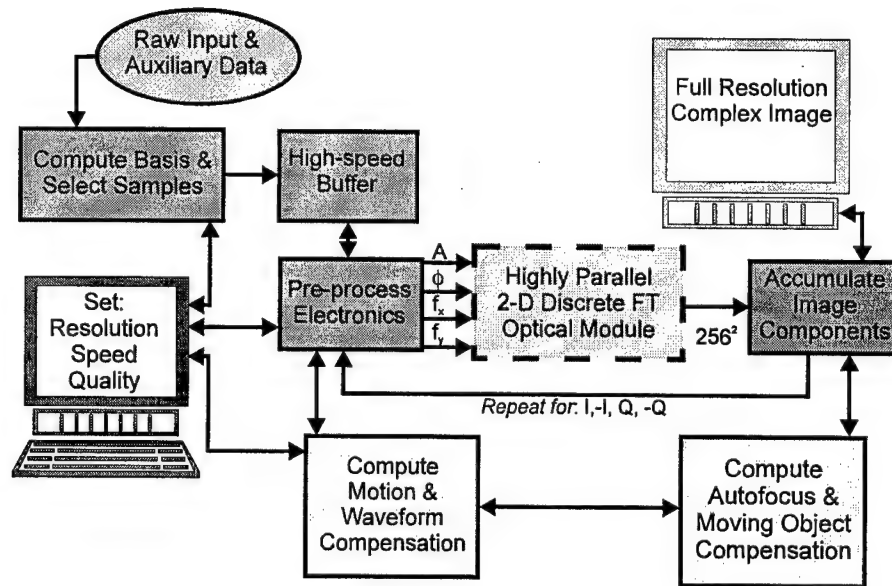
Figure 21: *ImSyn*™ SAR Processor Block Diagram

Based on a computer processing model, the results for size, weight and power requirements for the *ImSyn*™ Processor are shown in Table 17, below, and compared with those for i860 architectures.

	i860 Based	*ImSyn*™ (512 Model)	*ImSyn*™ (1024 Model)
Size (ft³)			
Current SAR	3.45	2.0*	n/a
Next Generation SAR	6.9	4.0	2.0
Weight (lb.)			
Current SAR	129	110*	n/a
Next Generation SAR	300	220	125
Power (watts)			
Current SAR	820	462*	n/a
Next Generation SAR	2200	924	725

Note: Processor greatly exceeds the image formation requirements.

Table 17: Comparison of i860 and *ImSyn*™ SAR Processors

Some performance characteristics for the *ImSyn*™ SAR Processor are given in Table 18. The commercial version mentioned is the current production model with a 256^2 photosensor.

	ImSyn™ Commercial	*ImSyn*™ (512 Model)	*ImSyn*™ (1024 Model)
Detector Size (pixels²)	256^2	512^2	1024^2
Dynamic Range	> 80 dB	> 90 dB	> 90 dB
Effective Input Rate	6.1 MHz	10.3 MHz	10.3 MHz
Output Rate	1.8 Mpixels/sec.	6.8 Mpixels/sec.	25 Mpixels/sec.

Table 18: Some Performance Characteristics of the *ImSyn*™ SAR Processor

We see that the *ImSyn*™ Processor meets or exceeds the requirements for current and next generation SAR at significant savings in space, weight and power consumption.

4. Task 3 - SAR ATR (SOW 4.1.3)

The purpose of this task was to study SAR image preprocessing requirements for target identification and discrimination when complex valued, spatially invariant filters are implemented on the *ImSyn*™ Processor. In fact, much more was achieved in that several sets of such filters were developed based on simulated SAR images and a high degree of correlation was demonstrated on the *ImSyn*™ breadboard. Before displaying these results, the theory of spatially invariant filters is briefly described.

4.1 Spatial Filters as a Mathematical Optimization

Using complex valued spatial filters to perform correlation functions leads to significantly more robust and versatile systems for pattern and target recognition. The additional degrees of freedom afforded by using both amplitude and phase information in either the image or frequency domains permits the design of filters incorporating a broader range of image variables, such as aspect angle, image scale and rotation, both improving correlation and providing increased rejection of false targets, thus yielding a higher probability of detection with a smaller search space.

To understand the implementation of these filters, let $\langle f, g \rangle$ denote the usual complex inner product on functions or arrays. If h is a complex function on R^2, define

$$h_x(y) = h(y\text{-}x).$$

So h_x is the function h translated to be centered at x. A good discriminant function h has the property that if f is an image, then $\left|\langle f, h_x \rangle\right|^2$ is relatively large if there is an object of interest in f near x and is relatively small otherwise.

Let F denotes the Fourier transform operator. It is an immediate consequence of Plancherel's Theorem that

$$\langle f, h_x \rangle = F^{-1}(F(f) \cdot F(h)^*)(x).$$

$F(h)^*$ is the spatial filter corresponding to the discriminant function h. This formula defines the correlation process and reveals the connection between optics and correlation.

Now, let $f_1,...,f_n,...,f_m$, the training set, be a finite sequence of images. The images are ordered so that $f_1,...,f_n$ are true targets, usually centered about the origin, and $f_{n+1},...,f_m$ are false targets. There will always be at least one true target but there need not be any false targets. The signal to clutter ratio of a discriminant function h (or, equivalently, the spatial filter $F(h)^*$) is defined to be

$$SCR(h) = T(h)/C(h)$$

where

$$T(h) = \min_{1 \le i \le n} \max_{x \in B_i} \left| \langle f_i, h_x \rangle \right|^2$$

and

$$C(h) = \max_{1 \le i \le m} \max_{x \in R_i} \left| \langle f_i, h_x \rangle \right|^2,$$

where B_i is any region in the correlation plane and R_i is a region in the correlation plane which contains at least the detector face and B_i.

$T(h)$ is called the *threshold* of h and $C(h)$ is called the *clutter* of h.

The process of deriving the correct spatial filters consists in maximizing $SCR(h)$. This is not a trivial exercise as $SCR(h)$ tends to be a highly nondifferentiable function of its many parameters. However, it can easily be shown[30] that maximizing $SCR(h)$ is equivalent to a standard quadratic programming problem and that is the approach taken here. Details about forming the spatial filters are given in Reference 31.

4.2 Results

Simulated SAR images were created using the Xpatch-ES code. The training sets consisted of twenty-one images each of a T-62 and a "generic" tank (an object having only tank like features) at several azimuth and elevation angles and four polarization combinations. Images were created for cases with no background and for a "perfectly conducting" ground plane.

Each of the images produced was represented as a 64 x 64 array of complex numbers. For each target, three such arrays were produced corresponding to the three polarization states of the measurements, hh, hv (= vh) and vv, where h and v refer to horizontal and vertical

51

polarization, respectively. Each of these images was first reflected about its diagonal for proper orientation and then changed to a nonnegative array by saving the magnitude of each entry. Each nonnegative array in turn was converted into a byte (256-bit) array simply by mapping each amplitude A to the integer nearest to 255A/M, where M is the maximum amplitude in the array. This effectively normalizes the radar returns from the targets and makes them easier to view.

At this point, there are now three 64 x 64 byte images corresponding to the three polarimetric measurements of the targets. Rather than choosing one image as most important or fusing all three of them into a single composite image by some ad hoc algorithm with a corresponding garbling of information, it was decided to create a tiled 128 x 128 byte image as follows. The hh byte image was placed in Quadrant II (northwest corner), the vv byte image was placed in Quadrant IV (southeast corner), the hv byte image was placed in Quadrant I (northeast corner) and the vh (= hv) byte image was placed in Quadrant III (southwest corner). This is analogous to the method employed in previous work[32].

Earlier research[33] has strongly suggested a definite advantage in recoding byte images into an array of phases when using correlation for target identification and discrimination. In that work, the byte image $\{a_{ij}\}$ was mapped to the array of phases $\{b_{ij}\}$, where $b_{ij} = \exp(\pi a_{ij}/255)$. The same recipe was followed here except when $a_{ij} = 0$, in which case $b_{ij} = 0$, i.e., only the nonzero bytes were phase encoded. As mentioned above, two sets of Xpatch-ES generated SAR tank images with no background and with a "perfectly conducting" ground plane were used in this study. Twenty-one of these images were of a T-62 at 45° elevation and centered at 90° + j*0.573°, j = -10, ..., -1, 0, 1, ..., 10. A second set of twenty-one SAR images of a generic tank were also created at the same elevation and azimuth angles. These sets of images are rather similar. Alternating these sets of similar tank images as true and false target training sets should provide a good test for filter design algorithms and their implementation in hardware.

Sample images without background are shown in Figure 22.

T-62   Generic Tank
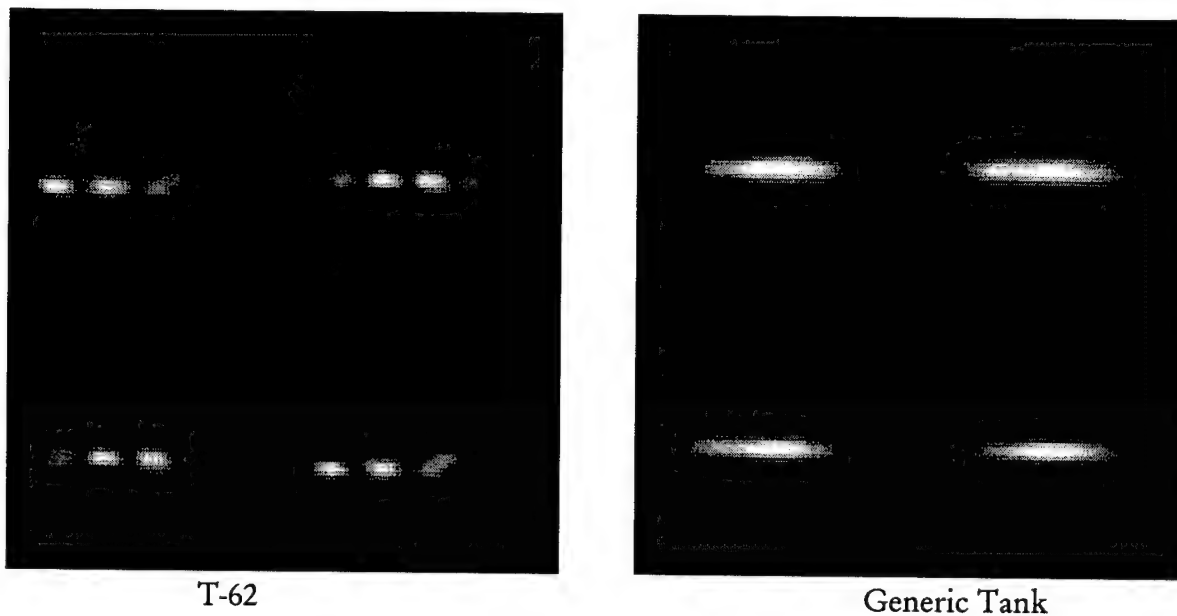
Figure 22: Xpatch SAR Images (No Background)

Returning to the Plancherel formula above, it is seen that the correlation surface should consist of a plot of the inverse Fourier transform of the product of the Fourier transforms of the spatial filter and the image (represented as a complex array). The Essex *ImSyn*™ Processor is especially suited to this type of computation. In Figures 23 and 24, correlation surfaces produced on the *ImSyn*™ breadboard are shown for the T-62 as a true target and the generic tank as a false target, respectively. The peak represents a gain of approximately 127.5.
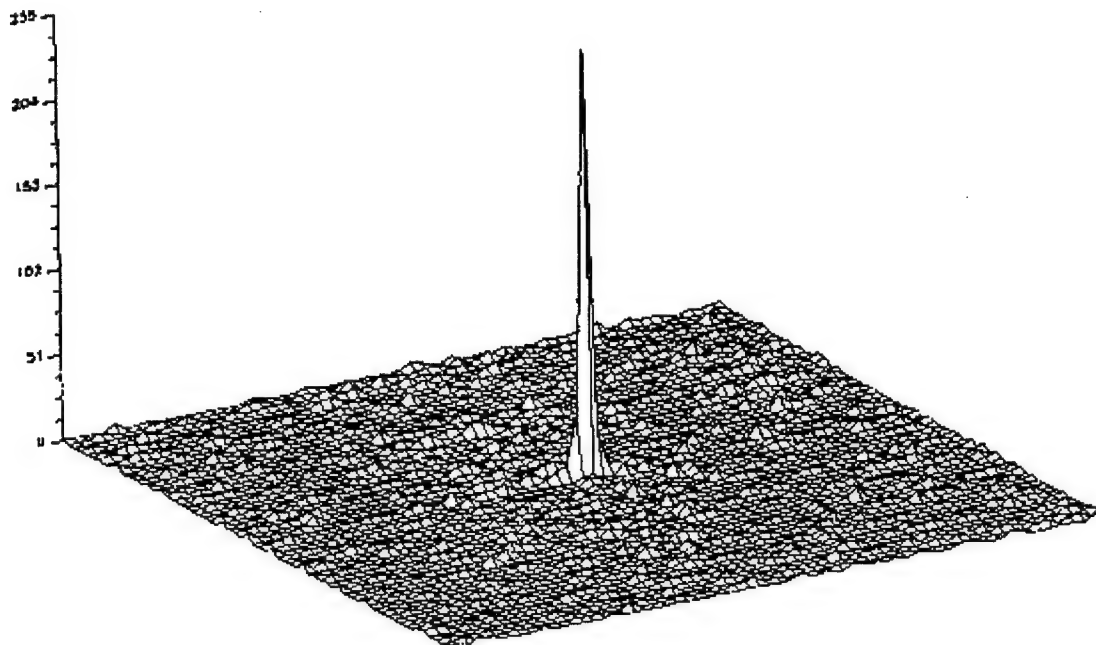
Figure 23: Correlation Surface for T-62 (True Target)
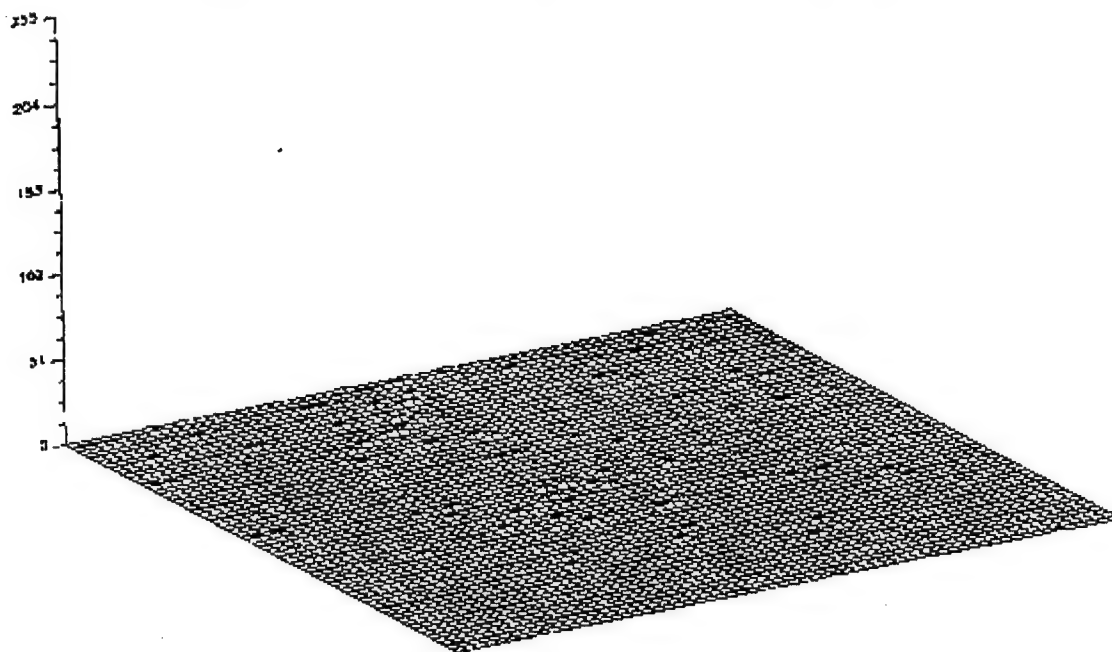
Figure 24: Correlation Surface for Generic Tank (False Target)

The Xpatch images for the same targets with a flat ground plane are shown in Figure 25.
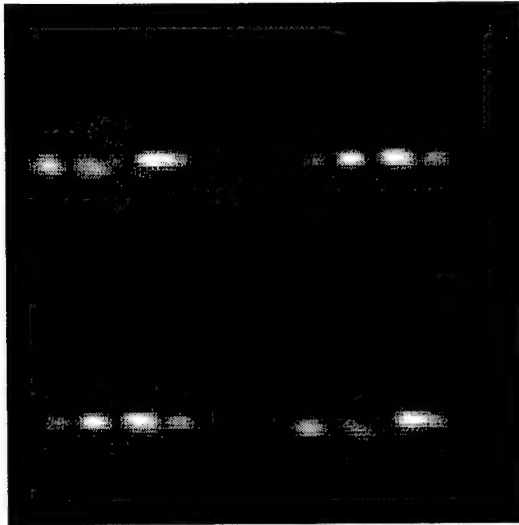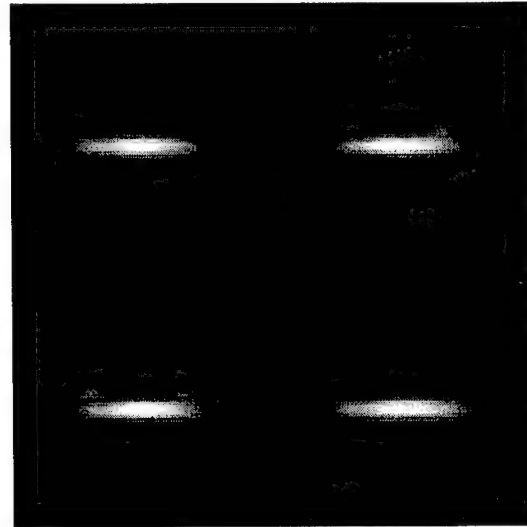
T-62   Generic Tank

Figure 25: Xpatch SAR Images (Flat Background)

The corresponding correlation surfaces are shown in Figures 26 and 27, representing a gain on the order of 100.
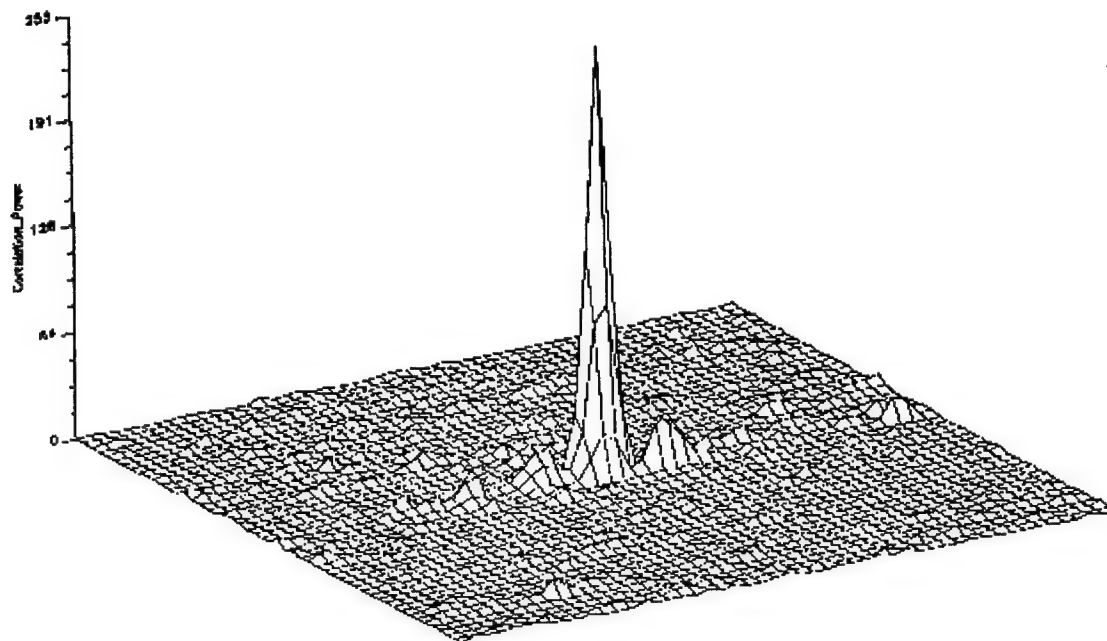
Figure 26: Correlation Surface for T-62 (True Target) with Background
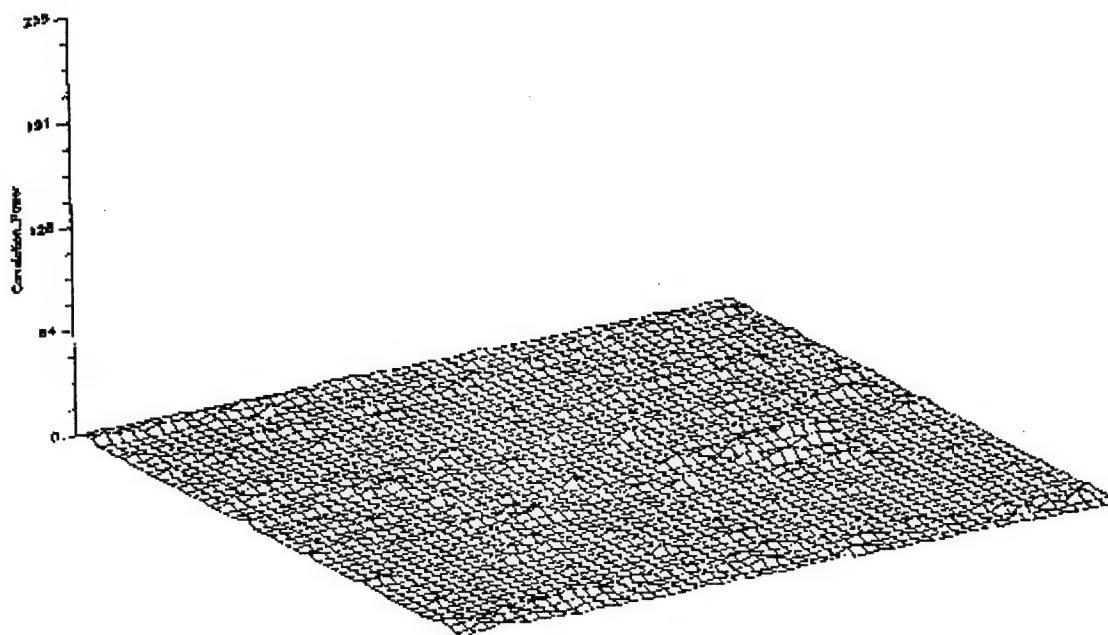
Figure 27: Correlation Surface for Generic Tank (False Target) with Background

Thus, although the background has some effect, a high degree of discrimination is still obtained.

The above results were obtained from rather small training sets of simulated SAR images and demonstrated on a breadboard version of the *ImSyn*™ Processor. Better performance could be expected from larger training sets and implementation on a production version of the processor which can perform more than 200 (128 x 128) or 800 (64 x 64) such correlations per second.

5. Task 4 - IR and Radar Search and Track (SOW 4.1.4)

This section describes an optical architecture to enhance the detection of sub-pixel moving targets in IR, radar or other imagery.

5.1 Introduction to the Problem

Faint subpixel targets in a fixed clutter background present a severe detection problem in IR and visible surveillance. If the targets are stationary with respect to the clutter, then increasing scene integration increases the signature of both the targets and fixed background by equal amounts, unless a filter can be applied to preferentially decrease the signature of the background relative to the targets. If, however, the targets are moving relative to the background, then the fixed clutter background can be more easily removed and a velocity filter applied to enhance the signature of targets of selected velocities.

Performing the velocity filtering over a wide range of velocities for the case that target velocities are unknown, e.g. in the case the target speeds are assumed to lie in a narrow range but the direction of target motion is unknown, is very computationally intensive when implemented on a digital computer. However, because of the speed and parallelism of optics, a simple optical processor can be designed to exhaustively search, in real time, for targets over a wide range of hypothesized velocities. Such an optical processor can be implemented that can easily keep up with a camera having a high frame rate. This section describes an architecture of an optical processor to implement the velocity filter to enhance the signatures of faint, subpixel moving targets in a clutter background.

5.2 Description of Approach

The problem addressed here is the detection of multiple faint subpixel targets moving in unknown directions over a background of clutter. An illustration of this problem is shown in Figure 28. An imaging array stares at a fixed ground location from a high altitude and outputs a sequence of image frames. These images consist of noise and signatures of the targets, if any targets are present. The noise consists of two components: fixed background clutter (such as terrain features, roads, lakes, clouds, etc.), which is correlated from frame to

frame, and time varying noise (such as IR detector noise), which is uncorrelated from frame to frame.

5.2.1 Frame Registration and Differencing

Figure 28 indicates that consecutive digitized image frames are registered relative to one another and differenced to remove background clutter prior to velocity filtering. Good registration is important since misregistration increases the fraction of clutter that is not removed in the differencing step and therefore leads to reduction in detectability.

In order that the frame differencing operation does not remove a moving target, it is necessary that the camera rate be no faster than will result in the target moving by one pixel per frame or that consecutive registered frames be added and that these summed frames be differenced.

OSTAN\DIOGEN_C.CV3
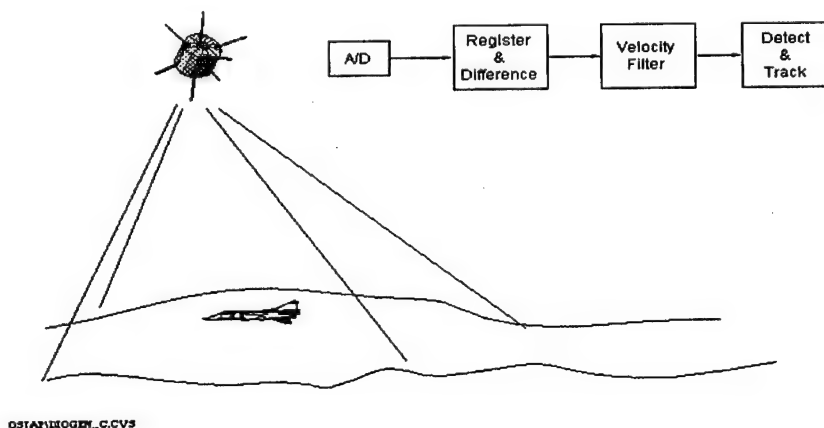
Figure 28: IR surveillance to detect subpixel moving targets.

5.2.2 Velocity Filtering

The next step after registration and differencing is to velocity filter the subtracted images. That is, the subtracted images are combined in such a way based on a hypothesized velocity so that the output signal to noise ratio of any targets moving at the hypothesized velocity will be increased relative to the input signal to noise ratio. If target velocity is unknown, then the velocity filter must be applied over a range of hypothesized velocities spanning the range of expected target velocities. The optical architecture to implement the velocity filter is illustrated in Figure 29.

The optical architecture is based upon a shift and add algorithm, i.e., a spatial domain velocity filter. For a given hypothesized velocity, a set of differenced images is shifted relative to one another with the magnitude and direction of the shift corresponding to the hypothesized velocity. The shifted difference images are summed together and, if there is a target moving through the images at the hypothesized velocity, the target signature in each of the difference frames will add into the same pixel of the sum image. Difference image pixels containing noise only will have both negative and positive values so that the expected value of pixels in the sum image which contain only noise is zero. On the other hand, the expected value of pixels in the differenced images which contain a target signature is positive so that the expected value of pixels in the sum image which contain a target signature is positive.

The resultant image is formed by comparing the sum images for each of the hypothesized target velocities and for each pixel keeping the maximum value that occurred within that pixel.
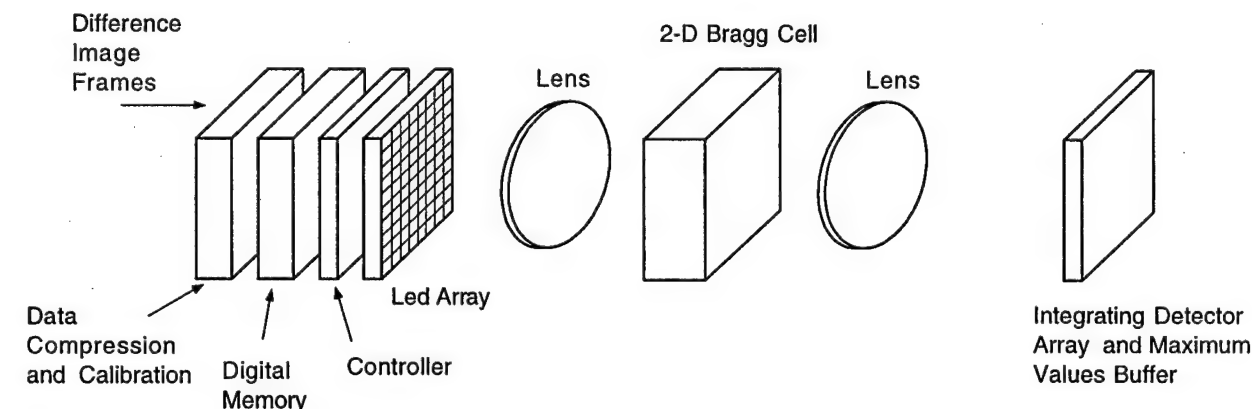
OSTAP\DIOGEN\DIOGEN.CVS

Figure 29: Optical architecture

After the set of difference images has been summed for each of the shift directions and the resultant image obtained, the oldest difference image is removed, the next difference image is input and the process of shifting and summing for each of the hypothesized velocities is repeated.

5.3 Discussion of Individual Component Availability

Through a custom development, similar devices are being developed for other applications.

5.3.1 Light Emitting Diode Array

The LED array, with accompanying memory and drive electronics, will require custom development. Each LED in the array is intensity modulated by an analog voltage from the

controller. A 30 dB dynamic range in intensity output is desired to be compatible with the expected dynamic range of the integrating detector array (photosensor). Each LED should also have a nearly equivalent response (output intensity vs. input voltage or current), however the controller will compensate for any differences.

The mean wavelength of the LED array should be in the 600 to 800 nanometer range to take advantage of existing LED array technology and to minimize total power required by the architecture. The Bragg cell's efficiency is best at the lower wavelength while the photosensor's responsivity will be a function of its design parameters and may peak toward the higher wavelength. A tradeoff needs to be performed to determine the optimum performance.

A microlens array may be necessary to collect as much of the rapidly diverging light from the array of LED's. There are numerous manufacturers of microlens arrays, hence this is not a critical component in this optical architecture.

5.3.2 Two-dimensional Bragg cell

The 2-D Bragg cell intended for use in this project is one which Essex has designed and currently is using in the commercial application of its *ImSyn™* Processor. This 2-D Bragg cell has a time-bandwidth product greater than 300 along each dimension which implies a resolution of 300x300. This 2-D cell, with minimal redesign of the input transducers, has been fabricated with a time-bandwidth product as high as 760 along each dimension.

5.3.3 CCD photosensor

The photosensor requires custom development to minimize the output data rate from the photosensor which is needed to perform the peak detection and hold function. This development can benefit from the experience being gained in the development of detectors with pixel level processing. Each pixel in the photosensor is required to accumulate charge (from incident photons at wavelengths for silicon response: 600 to 800 nanometers) over an specified integration period (standard sensor design techniques), compare and store the maximum value which occurs at a defined frame rate (custom design required), then output this maximum value. Hence, each pixel will require additional circuitry to accomplish this peak detection and storage function which may result in a "fill factor" reduction. Less than 100% of the photosensor area is actively available to detect light (see Figure 30).
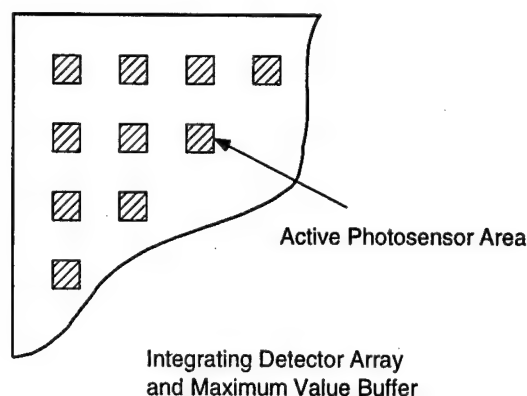
Figure 30: Custom photosensor array illustrating a low fill factor

A microlens array may be necessary to more effectively utilize the available light incident on the photosensor, thus minimizing the Bragg cell's RF drive power requirement and the output intensity from the LED array (or the efficiency of the microlens array collecting the light from the LED array). This is not critical, given the large number of manufacturers of microlens arrays.

5.4 Example of Expected Performance

The rate of velocity filtering is determined by the number and size of the difference frames, and by the bandwidth of the 2-D Bragg cell used for shifting the frames. For a Bragg cell bandwidth of 50 MHz, the time per difference frame versus frame size is:

Frame Size (pixels)	Frame time (microseconds)
45 x 45	3.0
90 x 90	4.9
256 x 256	11.5
512 x 512	21.7

Table 19: Time vs Frame Size

6. *Summary and Conclusions*

A Fourier transform based algorithm for solution of a class of linear systems important to STAP has been presented that is suitable for both all-digital and optoelectronic implementations. When combined with the optoelectronic architecture designed as part of

61

this effort, a system for computation of adaptive beam steering vectors appears that promises to be more than forty times faster than competing all-digital systems.

The *ImSyn*™ Processor, which has recently entered commercial production, has been shown to meet or exceed the requirements of current and next generation SAR with significant advantages in weight, size and power consumption. The advantages could be fully realized if an integrated sensor/processor development were investigated.

Complex valued spatial filters were developed for SAR images and were shown to provide a high degree of discrimination when implemented on the *ImSyn*™ Processor. The anticipated improvements in SAR resolution combined with the high speed of the *ImSyn*™ Processor and the economy of fully complex spatial filters show strong promise for SAR ATR. This could augment existing ATR techniques both with additional discrimination performance and as a computational accelerator.

Building on previous work on detection of subpixel moving targets, optical architectures for implementing the MERA algorithm were studied with specific reference to the ability to rapidly shift and add images. Off the shelf technology is available to implement such an algorithm, with the exception of the rapid image display component and a special 2-D detector. Although several potential applications were identified in IR and radar tracking, interest appeared to be low.

7. References

1. P. J. Davis, <u>Circulant Matrices</u>, John Wiley & Sons, New York, 1979.

2. Tony F. Chan, "An Optimal Circulant Preconditioner for Toeplitz Systems", *SIAM J. Sci. Stat. Comput.*, Vol. 9, pp. 766-771, No. 4, July, 1988.

3. Raymond H. Chan, James G. Nagy, Robert J. Plemmons, "Circulant Preconditioned Toeplitz Least Squares Iterations", *SIAM J. Matrix Anal. Appl.*, Vol. 15, No. 1, pp. 80-97, Jan., 1994.

4. J. Nagy, "Toeplitz Least Squares Computations", Ph.D. Thesis, North Carolina State University, Raleigh, NC, 1991.

5. J. Nagy, R. Plemmons, "Some Fast Toeplitz Least Squares Algorithms", *Proc. SPIE Conference on Advanced Signal Processing Algorithms, Architectures and Implementations II*, V1566, San Diego, CA, July, 1991.

6. M. Tismenentsky, "A Decomposition of Toeplitz Matrices and Optimal Circulant Preconditioning", *Linear Algebra and its Applications*, 154-156 (1991) pp. 105-121.

7. E. E. Tyrtyshnikov, "Optimal and Superoptimal Circulant Preconditioners", *SIAM J. Matrix Anal. Appl.*, Vol. 13, No. 2, pp. 459-473, April, 1992.

8. N. Y. Farhat, D. Psaltis, A. Prata, and E. Paek, "Optical implementation of the Hopfield model," Applied Optics, Vol. 24, pp 1469-14754, 1985.

9. D. Casasent, J. Smokelin, "New algorithm for analog optical matrix inversion", Applied Optics, 30, pp. 3281-3287, 1991.

10. H. J. Caulfield, J. Gruningher, J. E. Ludman, K. Steiglitz, H. Rabitz, J. Gelfant, and E. Tsoni, "Bimodal optical computers," Applied Optics, Vol 25, pp 3128 --, 1986.

11. M. A. G. Abushagur, H. J. Caulfield, "Optical Matrix Computations," Chapter 7 of Optical Processing and Computing, Edited by H.H. Arsenault, T. Szoplik, B. Macukow, Academic Press, Inc, 1989.

12. A. Spector, PIRI, private communication.

13. C. Zah., M. Amersfoort, B. Pathak , F. Favire , P. Lin , J. Gamelin , A. Rajhel , N. Andreadakis, R. Bhat, "High Performance Multiwavelength Integrated DFB Laser Arrays" DoD Photonics Conference Proceedings, pp.167-170, 1996.

14. Y. Z. Liu, Fermionics, private communication.

15. Y. C. Chen, UMBC Electrical Engineering Dept., private communication.

16. J. Laude, "Telecommunication networks using many channels grating WDM"; ISA technical document, 1996

17. M. Kawachi, NTT Tutorial at OFC, 1996.

18. "Terabit/second-transmission demonstrations make a splash at OFC 96," Laser Focus World, April 1996, pp. 13.

19. F. Bilodeau, D. Johnson, S. Theriault, B. Malo, J. Albert, K. Hill, "An all-fiber dense wavelength division multiplexer/demultiplexer using photo-imprinted Bragg gratings," IEEE Photonics Technology Letters, 7, pp. 388-390, 1995.

20. F. Bilodeau, K. Hill, B. Malo, D. Johnson, J. Albert, "High return loss narrowband all-fiber bandpass Bragg transmission filter," IEEE Photonics Technology Letters, 6, pp. 80-82, 1994.

21. Bernard Malo, Innovative Fibers, private communication.

22. Salim Juma, QPS Technologies, private communication.

23. L. Gesell, S. Evanko, "Continuously-Variable Time Delays from Photonics True Time Delay Beamforming Using Fiber Optic Resonators", Final Technical Report, RL-TR-96-32, Rome Laboratory

24. Y. Hibino, T. Kitagawa, K. Hill, F. Bilodeau, B. Malo, J. Albert, D. Johnson, "Wavelength Division Multiplexer with Photoinduced Bragg Gratings Fabricated in a Planar Lightwave Circuit Type Asymmetric Mach Zehnder Interferometer on Si," IEEE Photonics Tech. Letters, 8, pp. 84-86, 1996.

25. G. Kohnke, T. Erdogan, T. Strasser, A. White, M. Milbrodt, C. Henry, E. Laskowski, "Planar waveguide Mach-Zehnder bandpass filter fabricated with single exposure UV-induced gratings," OFC-96 Tech. Digest, pp. 277, 1996.

26. L. Gesell, S. Evanko, "Optical Resonators for True Time Delay Beam Steering", SPIE Proceedings, vol. 2749, paper no. 23.

27. S. Chandrasekhar, L. Garrett, L. Lunardi, A. Dentai, C. Burrus, C. Burrows, "Investigation of crosstalk performance of eight-channel pin/HBT OEIC photoreceiver array modules," IEEE Photonics Technology Letters, 8, pp. 682-684, 1996.

28. Robert M. Bowden, "IFP Sizing Analysis Final Report", 29 January, 1996.

29. William R. Franklin, "Optical Signal Processing at Essex Corporation", *Optical Engineering*, February, 1996.

30. Robert R. Kallman, "A General Optimization Algorithm Useful to Spatial Filter Design", *SPIE Proceedings on Advanced Signal Processing Algorithms, Architectures and Implementations VI*, vol. 2846, August, 1996.

31. William R. Franklin, "Advanced Sensor Signal Processing using Optical Techniques", *Progress Report #2*, 16 January, 1995.

32. Robert R. Kallman, "Invariant Phase Only Filters for TABILS24 Millimeter Wavelength Radar Data", *SPIE Proceedings*, volume 1960, pp. 74 - 90, April 1993.

33. Robert R. Kallman and Dennis H. Goldstein, "Phase Encoding Input Images for Optical Pattern Recognition", *Optical Engineering*, volume 332, number 6, June 1994, pp. 1806 - 1812.

DISTRIBUTION LIST

addresses	number of copies
PAUL L. REPAK ROME LABORATORY/OCPC 25 ELECTRONIC PKY ROME NY 13441-4515	5
ESSEX CORPORATION 9150 GUILFORD ROAD COLUMBIA MD 21046-1891	5
ROME LABORATORY/SUL TECHNICAL LIBRARY 26 ELECTRONIC PKY ROME NY 13441-4514	1
ATTENTION: DTIC-OCC DEFENSE TECHNICAL INFO CENTER 8725 JOHN J. KINGMAN ROAD, STE 0944 FT. BELVOIR, VA 22060-6218	2
ADVANCED RESEARCH PROJECTS AGENCY 3701 NORTH FAIRFAX DRIVE ARLINGTON VA 22203-1714	1
ATTN: RAYMOND TADROS GIDEP P.O. BOX 8000 CORONA CA 91718-8000	1
AFIT ACADEMIC LIBRARY/LDEE 2950 P STREET AREA B, BLDG 642 WRIGHT-PATTERSON AFB OH 45433-7765	1
ATTN: R.L. DENISON WRIGHT LABORATORY/MLPO, BLDG. 651 3005 P STREET, STE 6 WRIGHT-PATTERSON AFB OH 45433-7707	1

WRIGHT LABORATORY/MTM, BLDG 653   1
2977 P STREET, STE 6
WRIGHT-PATTERSON AFB OH 45433-7739

ATTN: GILBERT G. KUPERMAN   1
AL/CFHI, BLDG. 248
2255 H STREET
WRIGHT-PATTERSON AFB OH 45433-7022

US ARMY STRATEGIC DEFENSE COMMAND   1
CSSD-IM-PA
P.O. BOX 1500
HUNTSVILLE AL 35807-3801

NAVAL AIR WARFARE CENTER   1
6000 E. 21ST STREET
INDIANAPOLIS IN 46219-2189

COMMANDING OFFICER   1
NCCOSC RDT&E DIVISION
ATTN: TECHNICAL LIBRARY,CODE 0274
53560 HULL STREET
SAN DIEGO CA 92152-5001

COMMANDER, TECHNICAL LIBRARY   1
4747000/C0223
NAVAIRWARCENWPNDIV
1 ADMINISTRATION CIRCLE
CHINA LAKE CA 93555-6001

SPACE & NAVAL WARFARE SYSTEMS   2
COMMAND (PMW 178-1)
2451 CRYSTAL DRIVE
ARLINGTON VA 22245-5200

SPACE & NAVAL WARFARE SYSTEMS   1
COMMAND, EXECUTIVE DIRECTOR (PD13A)
ATTN: MR. CARL ANDRIANI
2451 CRYSTAL DRIVE
ARLINGTON VA 22245-5200

CDR, US ARMY MISSILE COMMAND   2
RSIC, BLDG. 4484
AMSMI-RD-CS-R, DOCS
REDSTONE ARSENAL AL 35898-5241

ADVISORY GROUP ON ELECTRON DEVICES   1
SUITE 500
1745 JEFFERSON DAVIS HIGHWAY
ARLINGTON VA 22202

REPORT COLLECTION, CIC-14   1
MS P364
LOS ALAMOS NATIONAL LABORATORY
LOS ALAMOS NM 87545

AEDC LIBRARY   1
TECHNICAL REPORTS FILE
100 KINDEL DRIVE, SUITE C211
ARNOLD AFB TN 37389-3211

COMMANDER   1
USAISC
ASHC-IMD-L, BLDG 61801
FT HUACHUCA AZ 85613-5000

AFIWC/MSO   1
102 HALL BLVD, STE 315
SAN ANTONIO TX 78243-7016

NSA/CSS   1
K1
FT MEADE MD 20755-6000

PHILLIPS LABORATORY   1
PL/TL (LIBRARY)
5 WRIGHT STREET
HANSCOM AFB MA 01731-3004

THE MITRE CORPORATION   1
ATTN: E. LADURE
D460
202 BURLINGTON RD
BEDFORD MA 01732

OUSD(P)/DTSA/OUTD   2
ATTN: PATRICK G. SULLIVAN, JR.
400 ARMY NAVY DRIVE
SUITE 300
ARLINGTON VA 22202

ROME LABORATORY/ERO   1
ATTN: RICHARD PAYNE
HANSCOM AFB, MA   01731-5000

ROME LABORATORY/EROC   1
ATTN: JOSEPH P. LORENZO, JR.
HANSCOM AFB, MA   01731-5000

ROME LABORATORY/EROP   1
ATTN: JOSEPH L. HORNER
HANSCOM AFB, MA   01731-5000

ROME LABORATORY/EROC   1
ATTN: RICHARD A. SOREF
HANSCOM AFB, MA   01731-5000

ROME LABORATORY/ERXE   1
ATTN: JOHN J. LARKIN
HANSCOM AFB, MA   01731-5000

ROME LABORATORY/ERDR   1
ATTN: DANIEL J. BURNS
525 BROOKS RD
ROME NY   13441-4505

ROME LABORATORY/IRAP   1
ATTN: ALBERT A. JAMBERDINO
32 HANGAR RD
ROME NY   13441-4114

ROME LABORATORY/OCP   1
ATTN: BRIAN M. HENDRICKSON
25 ELECTRONIC PKY
ROME NY   13441-4515

ROME LABORATORY/OCPC   1
ATTN: GREGORY J. ZAGAR
25 ELECTRONIC PKY
ROME NY 13441-4515

ROME LABORATORY/C3BC   1
ATTN: ROBERT L. KAMINSKI
525 BROOKS RD
ROME NY 13441-4505

ROME LABORATORY/OCP   1
ATTN: JAMES W. CUSACK
25 ELECTRONIC PKY
ROME NY 13441-4515

ROME LABORATORY/OCP   1
ATTN: JOANNE L. ROSSI
25 ELECTRONIC PKY
ROME NY 13441-4515

ROME LABORATORY/OCPA   1
ATTN: ANDREW R. PIRICH
25 ELECTRONIC PKY
ROME NY 13441-4515

ROME LABORATORY/OCP   1
ATTN: RICHARD J. MICHALAK
25 ELECTRONIC PKY
ROME NY 13441-4515

NY PHOTONIC DEVELOPMENT CORP   1
MVCC ROME CAMPUS
UPPER FLOYD AVE
ROME, NY 13440

MISSION OF ROME LABORATORY

Mission. The mission of Rome Laboratory is to advance the science and technologies of command, control, communications and intelligence and to transition them into systems to meet customer needs. To achieve this, Rome Lab:

a. Conducts vigorous research, development and test programs in all applicable technologies;

b. Transitions technology to current and future systems to improve operational capability, readiness, and supportability;

c. Provides a full range of technical support to Air Force Material Command product centers and other Air Force organizations;

d. Promotes transfer of technology to the private sector;

e. Maintains leading edge technological expertise in the areas of surveillance, communications, command and control, intelligence, reliability science, electro-magnetic technology, photonics, signal processing, and computational science.

The thrust areas of technical competence include: Surveillance, Communications, Command and Control, Intelligence, Signal Processing, Computer Science and Technology, Electromagnetic Technology, Photonics and Reliability Sciences.